Nanotechnology, Science and Applications

Dovepress
Taylor & Francis Group

Open Access Full Text Article

ORIGINAL RESEARCH

Three Noble Metal Nanoparticles Demonstrated Distinct Biological Interactions and Cell Death Pathways in Human Hepatocarcinoma Cell Lines

Kacper Wiktorowski[1,*], Kamila Podsiadło[1,*], Nasrin Abbasi Gharibkandi[2], Sylwia Michlewska[3], Katarzyna D Kania[4,5], Aleksander Bilewicz[3], Agnieszka Majkowska-Pilip[3], Marzena Szwed[1]

[1]Department of Medical Biophysics, Institute of Biophysics, Faculty of Biology and Environmental Protection, University of Lodz, Lodz, 90-236, Poland; [2]Institute of Nuclear Chemistry and Technology, Warsaw, Poland; [3]Laboratory of Microscopic Imaging and Specialized Biological Techniques, Faculty of Biology and Environmental Protection, University of Lodz, Lodz, 90-237, Poland; [4]Laboratory of Virology, Institute for Medical Biology, Polish Academy of Sciences, Lodz, 93-232, Poland; [5]Department of Diagnostic Techniques in Pathomorphology, Medical University of Lodz, Lodz, 92-213, Poland

*These authors contributed equally to this work

Correspondence: Marzena Szwed, Department of Medical Biophysics, Institute of Biophysics, Faculty of Biology and Environmental Protection, University of Lodz, Pomorska 141/143 St, Lodz, 90-236, Poland, Email marzena.szwed@biol.uni.lodz.pl

Purpose: New, more effective therapies are needed for patients with liver tumors who are ineligible for surgical resection, transplantation, or local ablation. Noble metal nanoparticles (NPs) exhibit substantial biological reactivity toward liver cancer cells, yet their unpredictable nanotoxicity highlights the need for a deeper understanding of NP-cell interactions. The present study examined the in vitro toxicological properties of gold (Au), palladium (Pd), and Pd-Au NPs in three hepatocellular carcinoma cell lines (HepG2, Hep3B, and Huh7D-12).

Methods: The cytotoxicity of noble-metal-based NPs was assessed using Alamar Blue and MTT colorimetric assays. Reactive oxygen species generation and oxidative stress markers were quantified by fluorometric, luminometric, and flow cytometry methods. Confocal microscopy combined with fluorescence readouts were used to evaluate mitochondrial homeostasis and programmed cell death pathways. Molecular markers of NP-induced cellular stress were further confirmed using qRT-PCR.

Results: Distinct cellular differences were observed among the three NPs, particularly in terms of cytotoxicity and death modalities. Au NPs caused mild mitochondrial perturbations without significant cytotoxicity. Pd NPs induced necroptosis, primarily at high concentrations. In contrast, Pd-Au NPs induced oxidative stress, lipid peroxidation, glutathione depletion, and transcriptional changes in the genes regulating glutathione synthesis and metabolism. Pd-Au NPs also activated ferroptosis, which is a regulated cell death pathway increasingly recognized as a promising anticancer strategy.

Conclusion: Among the tested formulations, Pd–Au NPs exhibited the strongest cytotoxic and antiproliferative effects that were driven by mitochondrial disruption and ferroptosis induction. These in vitro findings provided a mechanistic reason for advancing Pd-Au NP research efforts into in vivo studies and patient-derived preclinical models for hepatocellular carcinoma.

Keywords: nanoparticles, hepatocarcinoma, ferroptosis, oxidative stress, gold, palladium

Introduction

Hepatocellular carcinoma (HCC) is a devastating and highly lethal type of primary liver cancer and the most common adult gastrointestinal cancer.[1,2] It consists of a heterogeneous group of cells[3,4] with a variable proliferating potential, as well as areas of necrosis, hemorrhage, and infiltration into the normal liver tissue. Most HCC patients are diagnosed at advanced stages, at which point HCC is associated with a poor prognosis.[5] Additionally, HCC is resistant to chemotherapies, partly due to several drug resistance mechanisms, while systemic chemotherapy is generally ineffective.[1] High-dose therapies are often used when administering chemotherapy treatments. In contrast, low-dose therapies (also referred to as

https://doi.org/10.2147/NSA.S589907
Received: 9 January 2026
Accepted: 7 May 2026
Published: 3 June 2026

Graphical Abstract

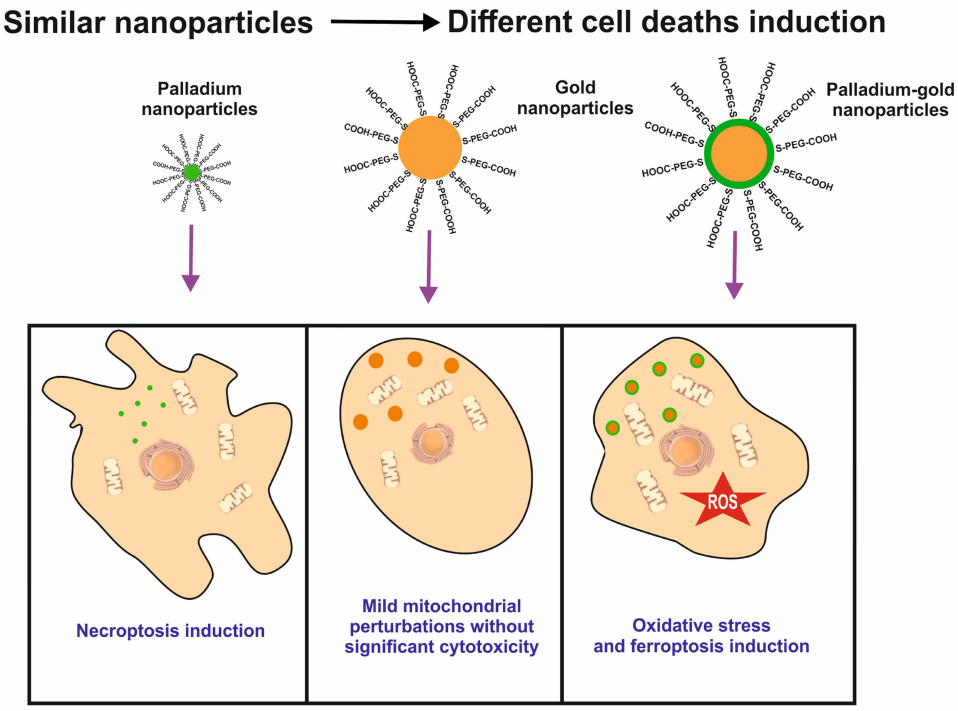

metronomic) can be effective while also reducing undesirable patient side effects.[4] For instance, the latest SHARP (Sorafenib Hepatocellular Carcinoma Assessment Randomized Protocol) and RESORCE (REgorafenib after SORafenib in patients with hepatoCEllular carcinoma) trials showed that sorafenib and regorafenib resulted in an overall delay in HCC progression of only up to 3 months.[6] Furthermore, liver transplantation is effective in the early or intermediate HCC stages, while surgical resection is difficult due to the rapid tumor recovery from infiltrating tumor cells. HCC stem cells are particularly resistant to the therapies mentioned above,[7] and the patient survival has not increased substantially.[8] Median survival times for HCC patients are between 6 and 11 months with standard treatments,[9] and the majority of advanced HCC patients die within 5 years of initial tumor diagnosis.[10,11]

Considering the irregularity of liver tumor vasculature and its increased permeability, the passive targeting and accumulation of ultra-small structures, such as nanoparticles (NPs), in HCC tissue are favored. The unique NP properties, such as their dimensions, ability to be tailored for specific functions, and enhanced drug delivery potential, make them a powerful tool in targeting liver cancer cells more effectively than traditional therapies are.[12] Additionally, NPs can be designed to carry chemotherapeutic drugs directly to tumor cells, thereby reducing damage to healthy tissues and minimizing side effects.[13] The medical branch of nanotechnology is continuously exploring different NP-based approaches, including liposomes, polymeric NPs, and inorganic NPs, for both imaging and targeted drug delivery.[14]

Metallic NPs have been widely used due to their efficiency in combating cancer progression and development, owing to their ease of synthesis and surface functionalization at the nanoscale range.[15,16] Among various noble metals, palladium (Pd) has been recognized as an element with remarkable stability and good catalytic and mechanical properties for application in brachytherapy of prostate cancer and choroidal melanoma.[17,18] To achieve a synergistic effect against tumors, Pd NPs are frequently combined with other metals, such as platinum or gold (Au), and engineered into core-shell structures, where one material (the core) is encapsulated by another material (the shell). This process enhances the catalytic activity and stability of Pd NPs, generates an interface between the core and shell, resulting in unique electronic effects known as ligand or strain effects, and improves NP stability after their interactions with biological fluids.[19,20]

Pd-based nanomaterials exhibit high electrocatalytic activity in the presence of hydrogen peroxide (H_2O_2), a metabolite that is produced at elevated levels by cancer cells within the tumor microenvironment.[21]

Pd NPs may interact with H_2O_2 through distinct catalytic pathways. Pd-catalyzed decomposition of H_2O_2 into water and molecular oxygen may contribute to the partial alleviation of tumor hypoxia, thereby potentially enhancing the efficacy of oxygen-dependent therapeutic modalities.[22] In addition, Pd NPs may also participate in Fenton-like redox reactions, leading to the generation of highly reactive oxygen species,[23] including hydroxyl radicals. This excessive reactive oxygen species (ROS) production disrupts redox homeostasis, damages cellular macromolecules, and activates regulated cell death pathways.

The resulting oxidative stress (OS)[24] may trigger classical apoptosis as well as ferroptosis, which is a form of regulated cell death that constitutes a promising, druggable cell death pathway in apoptosis-resistant tumors, including cancer types with a high likelihood of metastasis. However, little is known about whether the pro-oxidative properties of Pd-based nanomaterials are related to ROS-dependent nanotoxicity or iron-dependent cell death.

The present study therefore investigated the effects of Pd-based NPs on the viability of human liver cancer cell lines Hep3B, HepG2, and Huh7D-12. These cells lines have various susceptibilities to hepatitis B virus (HBV) and hepatitis C virus (HCV) infections,[25,26] express p53 protein differently,[27] and display diverse sensitivities to the Pd, Pd-Au, and Au NPs. The hepatoma cancer model was chosen because of its passive targeting utilization of the enhanced permeability and retention effect, as well as the leaky tumor vasculature. This phenomenon is specific to liver cancer cells. Thus, small-sized NPs can leave the bloodstream, pass through gaps in the endothelial lining of the vessels, and enter tumors, accumulating more effectively in the tumor microenvironment than in healthy, normal tissues.[28]

Our research group has published multiple articles evaluating the biological effects and efficacies of NPs containing radioisotopes in different cancer models.[29–32] Hence, it was interesting to conduct studies evaluating the cytotoxicity of non-radioactive NPs and the antiproliferative mechanism of pure nanomaterial by itself. The present study assessed the relationships between ROS-triggered toxicity of the examined NPs and the induction of programmed cell death pathways.

It was hypothesized that the OS generated by the tested forms of PD particles induced either necroptosis or ferroptosis differently. Numerous assays dedicated to cytotoxicity evaluation, including adenosine triphosphate (ATP) synthesis, cell membrane damage, metabolic activity, mitochondrial stability, ROS level production, lipid peroxidation, glutathione (GSH) depletion, cell membrane asymmetry, caspase-3/7 activity, and expression of genes involved in various cellular stress responses, were performed. The acquired knowledge of these mechanisms can be utilized to create future targeted therapies against HCC.

Materials and Methods

Materials

Gold (III) chloride trihydrate ($HAuCl_4 \cdot 3H_2O$), trisodium citrate dihydrate ($C_6H_9Na_3O_9$), palladium (II) chloride, thiolated polyethylene glycol (HS–PEG–COOH; 5 kDa), dihydroethidine, trisodium citrate dihydrate ($C_6H_9Na_3O_9$), phosphate-buffered saline (PBS), buthionine sulphoximine (BSO), Hoechst 33342, N-acetyl-l-cysteine (NAC), 3-(4,5-dimethylthiazol-2-yl)-2,5-diphenyltetrazolium bromide (MTT), resazurin, Antimycin A, MitoPQ, carbonyl cyanide p-trifluoromethoxy phenylhydrazone (FCCP), sodium chloride (NaCl), and TriPure Isolation Reagent were purchased from Sigma-Aldrich (St. Louis, MO, USA). SYBR Green, I Master Mix was from Roche (Roche Holding AG, Basel, Switzerland). Dulbecco's Modified Eagle's medium (DMEM) supplemented with GlutaMAX, trypsin-EDTA (ethylenediaminetetraacetic acid), a High-Capacity cDNA Reverse Transcription Kit, fetal bovine serum (FBS), penicillin/streptomycin, MitoSOX Red, DMSO (Dimethyl sulfoxide) (cell culture grade), C11-BODIPY, caspase-3/7 assay, and MitoTracker deep red FM were obtained from Thermo Fisher Scientific (Waltham, MA, USA), and JC-1 was from Abcam (Cambridge, London, UK). Well-described ferroptosis inhibitors liproxstatin (Lipro) and ferrostatin (Ferro)[33] were purchased from Cayman (Ann Arbor, MI, USA). GSH assay, RealTime-Glo Annexin V Apoptosis Assay, CellTox Green Cytotoxicity Assay, and Mitochondrial ToxGlo assay kits were purchased from Promega (Madison, WI, USA). The MycoAlert Mycoplasma Detection Kit was from Lonza (Walkersville, MD, USA). Milli-Q water was freshly

prepared using the Millipore Milli-Q Biocell purification system (Burlington, MA, USA). All chemicals were of analytical quality without further purification. Materials used for NP synthesis and other reagents are mentioned together with the description of the methods.

Preparation of Au, Pd, and Pd-Au NPs

The synthesis of Au NPs was conducted in an aqueous solution based on the modified procedure described by Turkevich et al[34] Core-shell NP synthesis was performed according to the method outlined by Wawrowicz et al[35] but using Na_2PdCl_4 instead of Na_2PtCl_6 and citrates as a reducing agent. The obtained Au NP solution was heated to 90°C for 10 min. Next, Na_2PdCl_4 (0.27 mg, 1 mM) and ascorbic acid (7.5 mg, 2 M) were added stepwise at 10-min and 30-min intervals. Subsequently, the reaction mixture was heated for 30 min at 90°C, cooled to room temperature, and finally characterized using transmission electron microscopy (TEM), dynamic light scatterin (DLS), and ultraviolet-visible (UV-Vis) techniques. PEGylated core-shell Au NPs were generated by the addition of HS-PEG-COOH (15,000 molar excess), stirred for 30 min at room temperature, and centrifuged at 9168 x *g*. Pd NPs were synthesized according to the modified method that was described previously.[36] Briefly, 5.3 mg of $PdCl_2$ was dissolved in HCl (1.2 M, 500 µL) and stirred at room temperature. Following dissolution, the Pd solution was diluted by adding 53.5 mL of H_2O. Subsequently, a freshly prepared $NaBH_4$ solution (3.5 M, 5 mL) was added to the mixture and stirred for 20 min. Finally, an aqueous solution of polyvinylpyrrolidone (PVP; 4.8 M, 21 mL) was added and stirred continuously for 1 h at room temperature.

The obtained Pd NPs were then stabilized by polyethylene glycol (PEG-COOH) chains. Specifically, the synthesized Pd NPs (5 nm) were combined with a 200 molar excess of HS-PEG-COOH (5 kDa) and stirred for 30 min. Then, the NPs were purified by centrifugation at 10,000 rpm for 10 min using Vivaspin 500 centrifugal filters with a 10,000 MWCO (Molecular Weight Cut-Off) polyethersulfone membrane. Considering the spherical shape, 5-nm NP diameter, and Pd density of 12.02 g/cm^3, the NP concentration was calculated to be ~2.9 x 10^{13} Pd NPs/mL.

Evaluation of Physicochemical Properties of NPs

TEM was used to evaluate the size and shape of NPs. First, 10 µL of all samples were vortexed, placed on 200 mesh copper grids with carbon surface, and incubated for 10 min. The samples were then stained with uranyl acetate-saturated solution for 20 min, washed in deionized water, and dried at room temperature. The TEM images were taken using a JEOL-1010 (JEOL Ltd., Tokyo, Japan). UV/Vis absorption spectra of Au, Pd, and Pd-Au NPs (1 mg/mL) were measured with a wavelength range of 200–1000 nm using the UV/Vis Varian spectrophotometer (Markham, ON, Canada). The size distribution and ζ-potential were determined using dynamic and electrophoretic light scattering (Zetasizer Nano ZS, Malvern Instruments, UK) in 0.01 M phosphate buffer at pH 7.4. The mean NP diameter (nm) was reported as the Z-average.

In vitro Cell Culture

HepG2 (ATCC, Manassas, VA, USA), Hep3B (ATCC, Manassas, VA, USA), and Huh7D-12 (Merck, Darmstadt, Germany) human HCC cells were cultured using high-glucose DMEM containing GlutaMAX (Thermo Fisher Scientific) supplemented with 10% FBS (Thermo Fisher Scientific),100 U/mL penicillin, and 100 g/mL streptomycin (Sigma-Aldrich) at 37°C in a 5% CO_2 humidified atmosphere. All cell lines were obtained from ATCC and were routinely tested for mycoplasma contamination using a MycoAlert Mycoplasma Detection Kit (Lonza).

Survival Studies

Cells growing in 96-well plates (6 x 10^3 cells/well) were incubated in a 5% (v/v) CO_2 humidified atmosphere with serial dilutions (0–140 µg/mL) of Au, Pd, and Pd-Au NPs for different periods of time as detailed in the figure captions. Cell toxicity was assessed by estimation of cellular enzymatic function utilizing Alamar Blue and MTT as enzymatic substrates. The absorbance (MTT assay) or fluorescence (Alamar Blue assay) readouts represented the percentage of the untreated control cells, and were expressed as the mean value of at least four parallel measurements ± standard deviation (SD). The IC_{50} values (concentration of NPs required for 50% growth inhibition) were determined in the tested hepatoma cell lines using GraphPad Prism 8.00 software (GraphPad Software Inc., San Diego, CA, USA).

MTT Test

Cell viability was assessed using the MTT assay at the end of the NP incubation periods (24, 48, and 72 h), when all the solutions from the treatment phase were replaced with a solution of 0.5 mg/mL MTT (Sigma-Aldrich) prepared in serum- and phenol red-free media as previously described.[37] The MTT-containing solution was then replaced with 100 µL/well of DMSO (POCH) after 4 h of incubation to dissolve the formazan crystals.[38] Finally, the absorbance measurements were performed at 580 nm using the Synergy HTX spectrophotometric plate reader (Thermo Fisher Scientific).

Alamar Blue Assay

The process of resazurin conversion to fluorescent resorufin was used to estimate the cellular enzymatic function. After the time-dependent incubation of cells with various NP concentrations, the cell medium was removed and replaced with 100 µL of serum and phenol-free DMEM containing resazurin (0.0125 mg/mL). Incubation was continued for an additional 3 h, and the fluorescence was then measured using a Fluoroskan Ascent FL microplate reader (Labsystem) with excitation and emission wavelengths of 530 nm and 590 nm, respectively.[39,40] Some experiments were performed in the presence of a reactive oxygen scavenger (NAC) or ferroptosis inhibitors (Lipro and Ferro). Next, the cells were preincubated for 1 h at 37°C with 5 mM NAC, 1 µM Lipro, and 2 µM Ferro before performing Alamar Blue measurements as described above.

Superoxide Generation

Intracellular ROS production was monitored by measuring the changes in dihydroethidium fluorescence, which appears blue after oxidation to ethidium in the cytosol and intercalation within the cellular DNA.[41] Briefly, cells were seeded into 96-well plates and incubated with the examined NPs at concentrations of 40, 60, and 100 µg/mL for up to 24, 48, and 72 h. Samples treated with Antimycin A (10 µM, 5 h of incubation in cellular growth conditions) were used as a positive control. The medium was then replaced with 100 µL/well of 5 µM dihydroethidium (DHE) (Sigma-Aldrich) prepared in FBS-free and phenol red-free DMEM. Next, the cells were incubated for 0.5 h at 37°C. The fluorescence of both dihydroethidium and ethidium was measured on a Fluoroskan Ascent FL microplate reader (Labsystem) using filter pairs of 355 nm/430 nm (dihydroethidium) and 355 nm/620 nm (ethidium).

Mitochondrial ROS Measurement

Mitochondrial ROS activity was measured with the MitoSOX Red assay, which utilizes a redox-sensitive fluorescent probe that is selectively targeted to the mitochondria.[42] Treatment with MitoPQ (30 µM, 24 h) was used as the positive control. The examined in vitro HCC cultures were treated with Au, Pd, and Pd-Au NPs (60 µg/mL) for up to 48 h. A fluorescent probe (MitoSOX Red; 5 µM) was added to each well and incubated for 45 min in cellular growth conditions. Fluorescence was measured using a Fluoroskan Ascent FL microplate reader (Labsystem) at an excitation wavelength of λ_{ex} = 390 nm and an emission wavelength of λ_{em}= 590 nm.

Mitochondrial Membrane Potential ($\Delta\psi m$)

HepG2, Hep3B, and Huh7D-12 cells were seeded into black 96-well titration microplates. NPs at different concentrations (40, 60, and 100 µg/mL) were added after 24 h and the cells were incubated for 24, 48, and 72 h. In parallel, the uncoupling mitochondrial agent FCCP used as a positive control was added to the wells for 4 h, consistent with previously published reports for other NPs.[40] The medium was removed at the end of the treatment, and the cells were incubated with 10 µM JC-1 in FBS- and phenol red-free DMEM for 20 min at 37°C in the dark. The probe was subsequently removed, and the cells were washed and resuspended in fresh DMEM. Following the 30-min incubation in cellular growth conditions, the fluorescence of both JC-1 monomers (λ_{ex} = 485 nm to λ_{em} = 530 nm) and dimers (λ_{ex} = 530 nm to λ_{em} = 590 nm) was measured with a Fluoroskan Ascent FL microplate reader (Labsystem). The data were presented as the ratio of dimer to monomer fluorescence in relation to the untreated control (fluorescence ratio taken as 100%).[43] JC-1 fluorescence images were obtained with an Olympus IX70 (Evident Scientific, Tokyo, Japan) fluorescence microscope immediately after the measurements.

DNA Content Estimation

DNA content was evaluated to avoid errors in the measurements of superoxide generation, mitochondrial membrane potential, and mitochondrial ROS levels caused by possible cell detachment, resulting in cell number decreases in the samples due to the drug treatment.[44] The probe was removed by gentle aspiration after measuring dihydroethidium fluorescence, and the plate was frozen at −70°C. The microplate containing cells was thawed at room temperature immediately before measurement. Then, 100 µL of deionized water was added to the appropriate wells, and the microplate with cells was refrozen at −70°C. After subsequent thawing, 100 µL of 0.25 µM Hoechst 33342 (PI) was added, and the DNA content of the plate was immediately measured using a Fluoroskan Ascent FL microplate reader (Labsystem).

RNA Isolation and RT-PCR Analysis

Total cellular RNA was isolated from HCC cells treated with the examined NPs (60 µg/mL) using TriPure Isolation Reagent (Sigma-Aldrich) according to the manufacturer's instructions. RNA was quantified and checked for purity, and 1 µg aliquots were then used to synthesize cDNA by reverse transcription (High-Capacity cDNA Reverse Transcription Kit; Thermo Fisher Scientific). Fragments specific to the genes of interest were amplified by PCR using the primer sequences shown in Table 1. Reactions were run on a Light Cycler 480 (Roche, Basel, Switzerland) using SYBR Green

Table 1 Primer Sequences Used for qRT-PCR

Gene	Strand	Sequence 5' → 3'
Hydroxymethylbilane synthase (*HMBS*)	Forward	GGCAATGCGGCTGCAA
	Reverse	GGGTACCCACGCGAATCAC
Hypoxanthine phosphoribosyltransferase (*HPRT1*)	Forward	TGACACTGGCAAAACAATGCA
	Reverse	GGTCCTTTTCACCAGCAAGCT
Retinoblastoma protein *(pRB)*	Forward	TGGATGGAGTATTGGGAGG
	Reverse	TCCAATTTGCTGAAGAGTGC
Myelocytomatosis *(Myc)*	Forward	CCTACCCTCTCAACGACAGC
	Reverse	GACTCTGACCTTTTGCCAGG
Catalase *(CAT)*	Forward	ACTTTGAGGTCACACATGACATT
	Reverse	CTGAACCCGATTCTCCAGCA
Glutaredoxin *(GLR)*	Forward	CCAACCACACTAACGAGATTCA
	Reverse	TCACTGCATCCGCCTATACAA
Glutathioneperoxidase (GPX1)	Forward	TTCCCGTGCAACCAGTTTG
	Reverse	TTCACCTCGCACTTCTCGAA
Bax	Forward	TGCCTCAGGATGCGTCCACCAA
	Reverse	CGGCAATCATCCTCTGCATGCTCCAT
Bcl-2	Forward	GCACGCTGGGAGAAAGGGTACGAT
	Reverse	CACATCTCCAGCATCCCACTCGTA
Superoxide dismutase (SOD)	Forward	AGGGCATCATCAATTTCGAG
	Reverse	TGCCTCTCTTCATCCTTTGG

I Master Mix (Roche) as described previously.[45] The housekeeping genes, hydroxymethylbilane synthase (*HMBS*) and hypoxanthine phosphoribosyltransferase 1 (*HPRT1*), were selected as the most suitable normalization parameters. The relative gene expression in the samples was calculated by the ΔCt method with the geometric mean of selected reference genes.

Lipid Peroxidation Detection

Lipid peroxidation was measured using the dye C11-BODIPY (581/591, Thermo Fisher Scientific). First, tert-Butyl hydroperoxide (tbOH; 200 μM, 2 h) was used as a positive control to determine whether the induced lipid peroxidation was monitored in the tested HCC cell lines. Second, cells treated with the investigated NPs for 48 h were labeled with C11-BODIPY (5 μM, 30 min) under the same conditions as those utilized for cell growth. The stained cells were subsequently harvested using trypsin (Sigma-Aldrich), centrifuged (400 x *g*, 5 min, 4°C), resuspended in PBS, and subjected to flow cytometry analysis.[37] The dye was excited using a 488-nm argon laser and evaluated with the PE A and FITC channels on an LSR II Flow Cytometer (BD Biosciences). At least 10,000 events were collected for each measurement.[46] The results were calculated as a ratio of oxidized probe to non-oxidized dye (a decrease in fluorescence intensity) with reference to the control fluorescence ratio.

GSH Measurement

The intracellular content of reduced GSH samples was determined using the GSH assay kit according to the manufacturer's procedure (Promega).[47] HepG2, Hep3B, and Huh7D-12 cells were seeded into 96-well titration microplates (1×10^5 cells). After 24 h, the cells were treated with 60 μg/mL of Au, Pd, and Pd-Au NPs for up to 48 h. After the treatment was completed, the medium containing the investigated compounds was replaced with 100 μL of GSH-Glo Reagent, and the plate was incubated at room temperature for 30 min. The exact volume of Luciferin Detection Reagent was subsequently added, and the incubation was continued for 15 min. The luminescence was measured in a Fluoroskan Ascent FL microplate reader (Labsystem). Inhibition of GSH synthesis by BSO (100 μM, 24 h) was used as a positive control for GSH depletion. The GSH content was calculated based on the standard curve prepared with GSH.

Mitochondrial ToxGlo Assay

The potential mitochondrial dysfunction due to NP exposure was quantified using the Mitochondrial ToxGlo assay (Promega). The assay is based on the differential measurement of biomarkers associated with changes in mitochondrial membrane integrity and cellular ATP level.[48] Cells were incubated in 96-well white plates with NPs (60 μg/mL) for 48 h at 37°C and 5% CO_2. Thereafter, half of the well volume was removed and replaced with an equal volume of the bis-AAF-R110 substrate (provided by the manufacturer). The plate was then incubated at 37°C for 30 min. The fluorescence of the bis-AAF-R110 substrate, which accumulated only in cells with disrupted membranes, was measured (λ_{ex} = 485 nm to λ_{em} = 520 nm). The plate was then equilibrated to room temperature, and an equal volume of the ATP component was added to each well. The plate was then gently shaken for 10 min at room temperature. The luminescence was measured via a Fluoroskan Ascent FL microplate reader (Labsystem) to evaluate the ATP level in NP-treated cells.[37] Samples treated with FCCP (100 μM, 4 h of incubation under cell growth conditions) were used as a positive control.

Confocal Microscopy

The general overview of mitochondrial health and function was carried out based on the MitoTracker deep red staining,[49] together with phalloidin and DAPI (4′,6-diamidino-2-phenylindole) fluorescent dyes. HepG2, Huh7D-12, and Hep3B cells grown in eight-chamber dishes (ibidi, Gräfelfing, Germany) were treated with Pd, Au, and Pd-Au NPs (60 and 100 μg/mL) for up to 48 h. Stock solutions (0.1 mM) of MitoTracker deep red (Thermo Scientific) were diluted to a 100-nM working solution with RPMI (Roswell Park Memorial Institute) culture medium and added directly to the HCC cell culture in the absence of the particles. After incubation with MitoTracker deep red working solution for 30 min at 37°C, the cells were washed with PBS, fixed in a 4% (w/v) paraformaldehyde solution at room temperature (Thermo Fisher Scientific) for 15 min, and permeabilized in 0.2% (w/v) Triton-X 100 solution (0.2% (w/v)) in PBS for 10 min at room

temperature. The cells were subsequently incubated with Phalloidin Alexa Fluor 488 (Thermo Fisher Scientific) diluted at a ratio of 1:400 in PBS for 30 min at room temperature. The cells were washed three times with PBS for 5 min each time and then stained with the nuclear staining reagent, DAPI (1 μg/mL) for 5 min at room temperature. A detailed cellular analysis was performed using confocal microscopy (Leica TCS SP8, Leica Microsystems, Wetzlar, Germany). A total of 15 raw images per plane were collected for image quantification. The fluorescence intensity was calculated using Leica Application Suite X (Leica Microsystems, Wetzlar, Germany).

Caspase-3/7 Assay

The activities of caspases-3 and −7 were estimated using the CellEvent Caspase-3/7 Green Detection Reagent (Thermo Fisher Scientific) according to the manufacturer's protocol.[50] The cells were seeded into 96-well black plates (10 x 10^3 cells/well). After 24 h, incubation with NPs (60 μg/mL) was performed for 48 h. The cells were then labeled with CellEvent Caspase-3/7 Green Detection Reagent (5 μM) diluted in PBS with 5% FBS to minimize fluorescence background. Fluorescence of the stained samples was measured using a Fluoroskan Ascent FL plate reader (Labsystem). The samples that showed a significant increase in fluorescence were also pretreated with pan-caspase inhibitor z-VAD (20 μM).

Apoptosis and Necroptosis Assay

Phosphatidylserine externalization was measured for the detection of early-stage apoptosis and was determined using a luminescence signal. In parallel, the cell membrane integrity was monitored based on fluorescence staining as a marker of necroptotic cell death. It was possible to evaluate both cell death types by carrying out the RealTime-Glo Annexin V Apoptosis Assay (Promega, Madison, WI, USA).[51] HepG2, Hep3B, and Huh7D-12 cells (1.5 x 10^4 cells/well) were seeded into 96-well white microplates. The investigated NPs (100 μg/mL) were added to the wells after 24 h, and the incubation was continued in cell growth conditions (37°C, 5% CO_2) for the next 48 h. The medium was removed at the end of the treatment, and the cells were incubated in the dark with detection reagent that was prepared by mixing Annexin V NanoBiT Substrate, $CaCl_2$, Necroptosis Detection Reagent, Annexin V-SmBiT, and Annexin V-LgBiT supplied by the kit manufacturer (Promega). After mixing, the plate was incubated for 30 min at 37°C. Finally, the luminescence and fluorescence (λ_{ex} = 485 nm, λ_{em} = 530 nm) of apoptosis and necroptosis markers, respectively, were measured on a Fluoroskan Ascent FL microplate reader (Labsystem).

Cell Death Assay and Studies Using Ferroptosis Inhibitors

Cell death was assessed using the CellTox Green Cytotoxicity Assay (Promega), which measures the changes in membrane integrity that occur during cell death.[52] The assay system utilizes a proprietary asymmetric cyanine dye (excluded from viable cells) that preferentially stains the DNA of dead cells. HepG2, Hep3B, and Huh7D-12 cells were incubated in DMEM containing NPs (60 μg/mL) for 48 h at 37°C and 5% CO_2. For ferroptosis studies, the cells were also preincubated for 1 h at 37°C with either Lipro (1 μM) or Ferro (2 μM) before a further incubation for 24 h with NPs, as performed in a previous study.[37] Half of the NPs solution volume was removed when the NP treatment was complete, replaced with an equal volume of Combine CellTox Green Dye, and gently mixed for 15 min at room temperature in the dark. Fluorescence intensity was monitored with Fluoroskan Ascent FL plate reader (Labsystem) with excitation and emission wavelengths of 485 nm and 528 nm, respectively.

Statistical Analysis

All measurements were performed in at least duplicate, and each experimental method was repeated using cells from a minimum of three independent passages ($n \geq 3$). Data were presented as mean ± SD. Statistical analyses were carried out using GraphPad Prism version 8.0 (GraphPad Software Inc., San Diego, CA, USA). The Shapiro–Wilk test was used to assess the normality of data distribution, and the Brown-Forsythe test was used to evaluate the homogeneity of variances. ANOVA followed by Tukey's post hoc test for multiple comparisons was used when assumptions of normality and equal variance were met. The results for cells treated with Pd and Pd-Au NPs were compared for data obtained

during qRT-PCR measurements. A two-tailed unpaired Student's *t*-test with Bonferroni correction was performed. A P-value of $P < 0.05$ was considered statistically significant.

Results

Pd and Pd-Au NP Synthesis and Characterization

Pd was successfully deposited on 15-nm Au NPs, achieving a yield of >95%. The process involved a gradual and controlled deposition of reduced Pd, followed by the rapid diffusion of Pd metal through the surface of Au NPs. This method obtained a homogeneous and thin Pd layer on the surface of Au NPs, similar to the results described in a previous publication.[35] The calculation based on the decrease in the number of Pd ions in solution after adding Au NPs indicated that Au NPs were coated with an average of seven Pd atom layers. Furthermore, the total thickness of Pd layers did not exceed 2 nm. The TEM results of the synthesized Pd NPs indicated that these particles were approximately 5 nm in size, while the Pd-Au NPs were sized about 17 nm. PVP molecules were entirely replaced on the surface of Pd NPs by PEG-thiol molecules due to the strong attraction between thiol groups and Pd atoms. The synthesized PEGylated NPs were stable in solution, as the layer of PEG molecules on the surface created an electrostatic repulsion force due to the electric double layer.

Noble Metal Particle Characterization

Ultra-small Pd and Pd-Au NPs with a Pd-enriched surface were examined to investigate whether Pd-based core-shell NPs exhibited similar properties and biological activities. The obtained results were compared with those where Au NPs were used as a control sample (Figure 1A). TEM outcomes confirmed their spherical morphology and high dispersity (Figure 1B). Quantitative analysis performed during TEM evaluations revealed mean diameters of approximately 11 nm for Au NPs, 12 nm for Pd-Au NPs, and 6 nm for Pd NPs (Figure 1C). The size, polydispersity index (PDI), and ζ-potential of the tested NPs were also measured. The hydrodynamic diameter of particles assessed by DLS analysis was in the range of 93–152 nm, with a size distribution (PDI) below 0.5. Pd, Au, and Pd-Au NPs had a negative charge with a ζ-potential of −11 mV (Table 2). Complementary UV-Vis spectroscopy results showed a distinct absorption peak at 531 nm exclusively for Au NPs, consistent with their plasmonic properties (Figure 1D).

Pd-Based Particles Exerted Differential Cytotoxicity

Analysis of the Au, Pd, and Pd-Au NP cytotoxicity was performed using the MTT assay to determine the cellular metabolic activity and Alamar Blue assay to measure the reduction of resazurin to resorufin after 24, 48, and 72 h of incubation with the three different HCC cell lines (Hep3B, HepG2, and Huh7D-12; Figure 2A and B). These analyses revealed that Pd-Au core-shells were much more toxic to liver cancer cells than Pd or Au NPs. The cytotoxic effect of Pd-Au particles increased over time with incubation with the examined substance. Both the MTT and Alamar Blue assay results provided compelling evidence that the effect of Au NPs was 10-fold less toxic than that of Pd-Au NPs. Importantly, the effect of Au and Pd NPs assessed by the Alamar Blue assay after 72 h of incubation with NPs revealed a similar nonsignificant reduction in cellular viability in all tested HCC lines. Additionally, the cytotoxic effect of Pd NPs was diminished compared to the data obtained during the MTT assay. For example, the Alamar Blue assay revealed 31%, 14%, and 6% reductions in viabilities of Hep3B, HepG2, and Huh7D-12 cells, respectively, following the treatment with 140 μg/mL Pd NPs for up to 72 h. In contrast, MTT data showed decreases that were approximately 2–3 times higher.

Both of the performed cytotoxicity assays were able to estimate the respective Pd-Au NP IC_{50} values (Table 3). A comparison of IC_{50} concentrations showed that Huh7D-12 cells were the most resistant among the tested liver cancer cell lines, whereas HepG2 and Hep3B demonstrated similar sensitivities with IC_{50} values in the range of 65–68 μg/mL. These parameters were also calculated for Pd NPs. However, the obtained values were outside the range of the particle concentrations used for this assessment and should be considered non-significant.

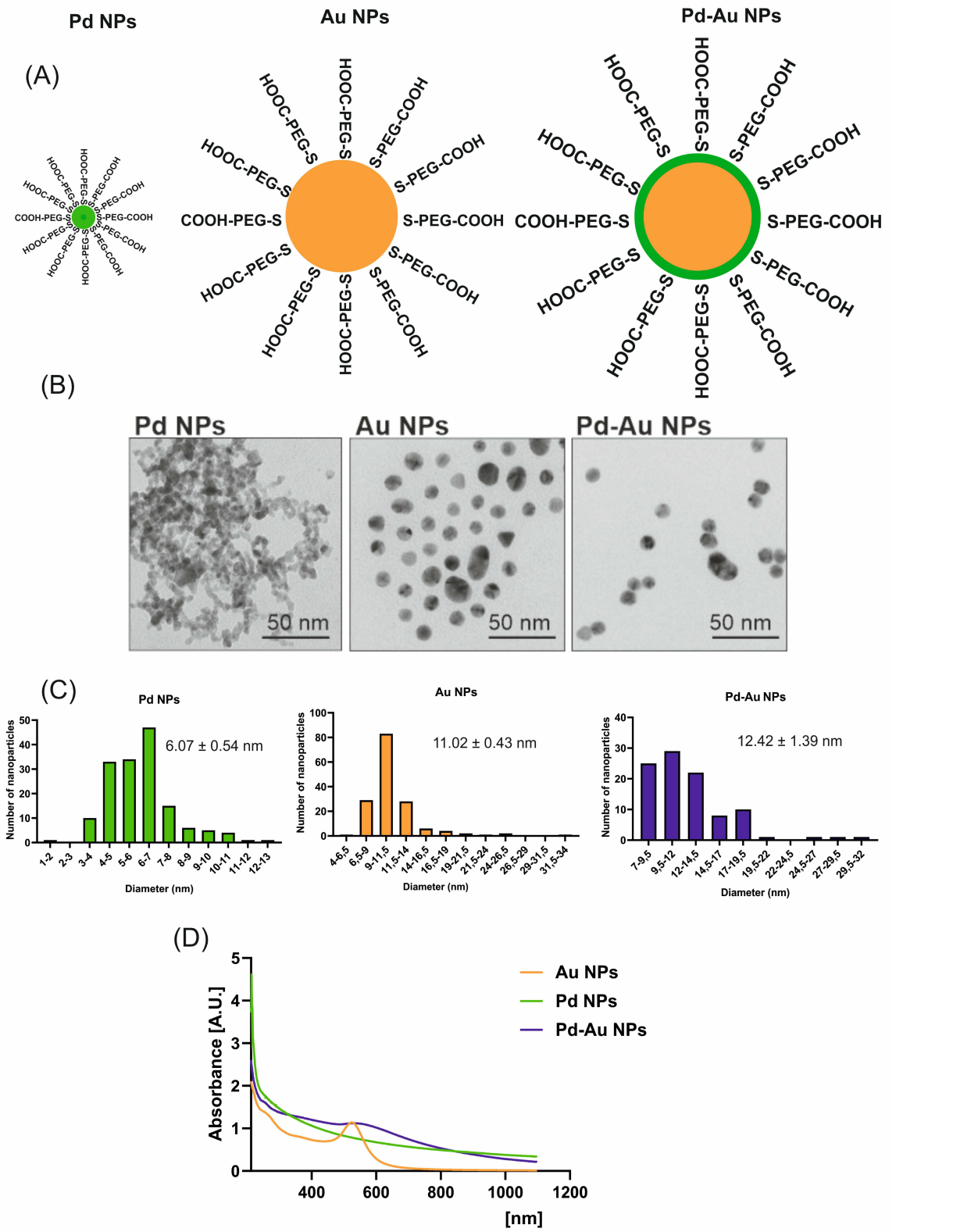

Figure 1 Physicochemical characteristics of metal nanoparticles (NPs) used in the study. (**A**) Simplified structure of Pd, Au, and Pd-Au NPs. (**B**) Electron micrographs of tested NPs. Magnification of 150,000x was used to examine the NPs, bar = 50 nm. (**C**) Gaussian distribution of Pd, Au, and Pd-Au NP size calculated based on TEM images; the mean diameter was calculated for three independently synthesized NP solutions. (**D**) UV/Vis absorption spectra for Au, Pd, and Pd-Au NPs.

https://doi.org/10.2147/NSA.S589907

Table 2 Physicochemical Properties of Investigated Particles: Size Distribution, Zeta-Potential, and PDI. DLS Measurements Were Performed Using a Malvern Zetasizer Nano ZS (Mean ± SD, n = 3)

Nanoparticles	NP Size (nm)	PDI	Z-Potential (mV)
Pd NPs	154.4 ± 106	0.50± 0.20	−13.0 ± 3.0
Au NPs	98.4 ± 91.2	0.30 ± 0.10	−11.0 ± 3.2
Pd-Au NPs	93.3 ± 15.6	0.30 ± 0.20	−14.4 ± 3.1

Generation of Intracellular ROS by Pd-Based Particles

Previous studies reported that diverse classes of NPs elicit cytotoxic effects in cancer cells via ROS generation, culminating in cellular injury and apoptotic cell death.[53–55] Thus, intracellular ROS production induced by Au, Pd, and Pd-Au NPs was assessed in a time- (24, 48, and 72 h) and concentration-dependent (40, 60, and 100 µg/mL) manner. The level of free radical generation was evaluated by using the ROS probe, and dihydroethidium, which formed a red fluorescent product 2-hydroxy ethidium upon specific reaction with superoxide radical ($O2^{-\bullet}$).[42] Annamycin A (AMA) served as a positive control for inducing OS, triggering a 1.3-fold increase in ROS production in HCC cell lines (Figure 3A). To validate the hypothesis that ROS production was involved in NP toxicity, the cells were pretreated with 5 mM NAC before incubation with the examined substances. No ROS production was observed in Au NP-treated cells (Figure 3B). This indicated that Au NPs used in the present study did not induce intracellular ROS production. A similar observation was made for Hep3B and Huh7D-12 cell lines treated with Pd NPs. The exception (1.5-fold growth) was noted for HepG2 cells exposed to Pd particles (100 µg/mL) for up to 48 h. Here, ROS generation in liver-derived cells was maximal after 72 h of treatment with Pd-Au NPs and increased approximately 4-fold in all examined hepatocarcinoma cell lines. Additionally, HepG2 cells showed a predominant susceptibility to ROS production triggered by Pd-Au core-shells. All examined NP concentrations caused abnormal superoxide radical production after 24 and 48 h of incubation under the cellular growth conditions. Furthermore, preincubation with NAC effectively diminished the Pd-Au NP-induced increases in ROS levels. Importantly, the same experimental conditions (preincubation of hepatocarcinoma-derived cells with antioxidant 5 mM NAC) resulted in a partial protection from Pd-based NPs when cell viability

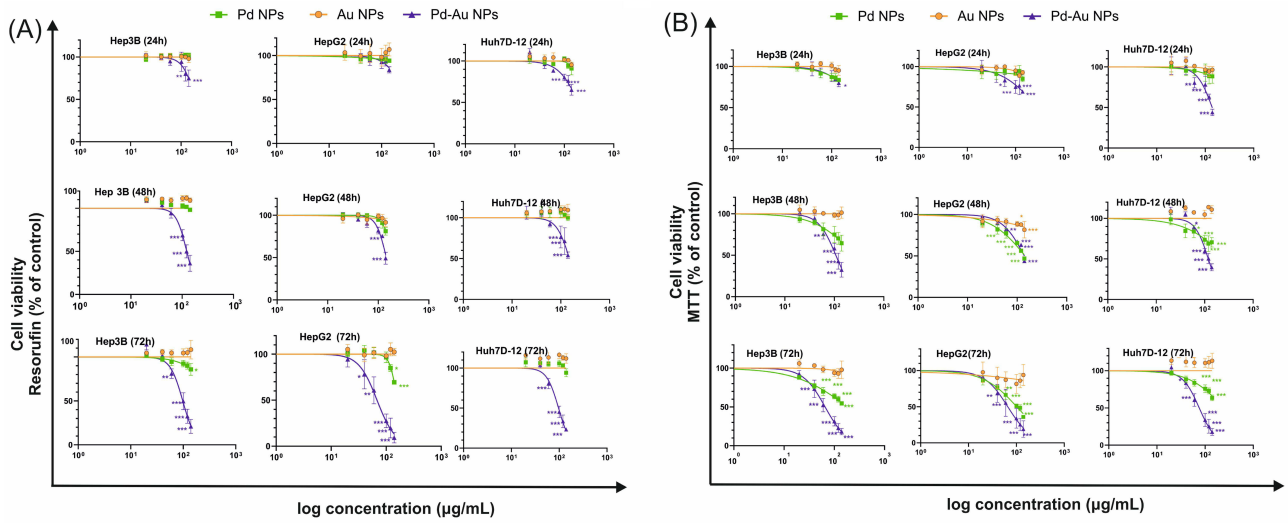

Figure 2 Cytotoxic effect of Au, Pd, and Pd-Au NPs on human hepatocarcinoma cell lines. HepG2, Hep3B, and Huh7D-12 cell viability was measured using (**A**) Alamar Blue or (**B**) MTT assays after incubation for 24, 48, and 72 h with increasing concentrations of tested NPs. Data are presented as a percentage of untreated control cells, with the mean ± SD, n = 4. *P < 0.05, **P < 0.01, and ***P < 0.001 for comparison with untreated control cells.

https://doi.org/10.2147/NSA.S589907

Table 3 IC_{50} Values for Au, Pd, and Pd-Au NPs Examined in vitro in Hepatocarcinoma Cells, Calculated from Cell Viability Curves

Cell Line	NP Type	Alamar Blue Assay		MTT Assay	
		IC_{50} (μg/mL)	95% Confidence Interval (μg/mL)	IC_{50} (μg/mL)	95% Confidence Interval (μg/mL)
Hep3B	Pd	437.1	248.8–1271	183.3	159.2–220.7
	Au	Not reached	–	Not reached	–
	Pd-Au	98.0	91.5–104.3	65.5	63.2–67.9
HepG2	Pd	163.0	154.3–178.0	101.8	91.5–115.0
	Au	Not reached	–	Not reached	–
	Pd-Au	68.2	61.8–74.9	66.2	62.5–70.0
Huh7D-12	Pd	Not reached	–	242.8	195.4–340.4
	Au	Not reached	–	Not reached	–
	Pd-Au	97.0	91.0–103.9	75.6	68.4–83.2

Notes: IC_{50} values for Au NPs could not be determined because 50% inhibition was not achieved within the tested concentration range.

was measured using the Alamar Blue assay after 48 and 72 h of incubation with particles (Figure 3C). This phenomenon, however, was observed only in core-shell-treated cells (~15–70%), but not in Pd NP cytotoxicity (~5%).

The ROS burst observed here, primarily following the application of Pd-Au NPs, can cause damage to cellular structures and disrupt the normal physiological cell functions. To counteract the oxidative damage inflicted by ROS on cellular constituents, such as carbohydrates, nucleic acids, unsaturated lipids, and proteins, cells upregulate a diverse repertoire of antioxidant enzymes.[56,57]

Hence, the effect of noble metal-based NPs on the transcription of primary enzymatic antioxidants, such as catalase (CAT), superoxide dismutase (SOD), and thioredoxin (TXN), involved in protecting cells against OS was estimated. The level of mRNA transcription determined in HCC cells incubated with particles (60 μg/mL) for 48 h revealed the most significant changes in ROS levels (Figure 3B). Results for NP-treated cells were standardized to the level of mRNA transcription in untreated (control) cells, which was considered to be 1. Pd-Au NPs upregulated *SOD* and *TXN* transcriptions in Hep3B cells, whereas HepG2 cells exhibited increased mRNA levels of *CAT* and *SOD* (Figure 3D). The difference between cells treated with Pd NPs and those exposed to Pd-Au core-shells was statistically significant only for *TXN* transcription in Hep3B cells, where expression was at least 1.25-fold higher following the treatment with either nanopalladium formulation. In contrast, *CAT* transcription was downregulated in Hep3B cells exposed to Pd (0.78-fold) or Pd-Au (0.47-fold) NPs. In Huh7D-12 cells, among the antioxidant enzymes analyzed, only *TXN* transcription was elevated (1.8-fold) after incubation with Pd-Au core-shells.

A disruption in cellular redox balance often involves lipid peroxidation, which is the oxidative degradation of polyunsaturated fatty acids. The lipophilic fluorescent probe, BODIPY 581/591 C11, which shifts its fluorescence emission from red (590 nm, PI filter) to green (510 nm/ FITC filter) upon oxidation, was used to assess lipid peroxidation in the present study. The ratio of red-to-green fluorescence was calculated (Figure 4A). In addition, tbOH was used as a positive control for inducing rapid lipid peroxidation. Consequently, 2- and 3-fold decreases in PI/FITC ratios in Hep3B, HepG2, and Huh7D-12 cells were observed. Flow cytometry histogram analysis results revealed a significant increase in the oxidized form of the BODIPY 581/591 C11 probe (Figure 4B) when HCC cells were exposed to Pd-Au NPs. The most visible lipid peroxidation was recorded in Hep3B (29.4) and HepG2 (39.7) cell lines. Importantly, lipid peroxidation was almost entirely inhibited in cells preincubated with NAC.

The prevention of cellular compartment oxidation may have been possible if the pool of the main cellular antioxidant GSH was not diminished and homeostasis of enzymes involved in GSH synthesis was not disturbed. Because pretreatment of cells with NAC, which is necessary for GSH production, had a rescued effect against Pd-Au NP cytotoxicity, it

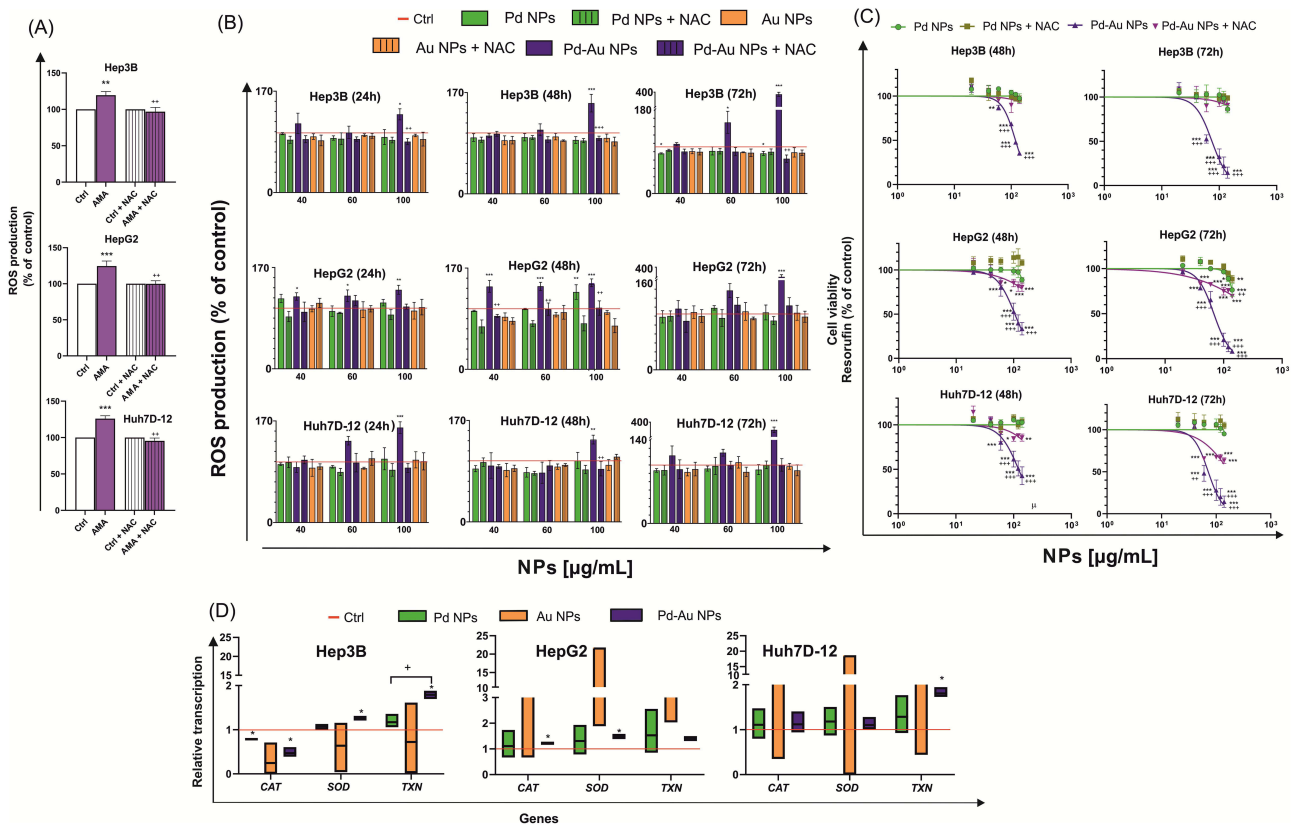

Figure 3 ROS production mediates the cytotoxicity of NPs. (**A**) Effect on ROS production after cell incubation at 37°C with 10 µM AMA (Antimycin A) for 5 h as a positive control. Bars represent mean values ± SD from three independent experiments. $^{**}P < 0.01$; $^{***}P < 0.001$ for comparison with data obtained in the absence of AMA and $^{++}P < 0.01$ for comparison with cells preincubated with NAC. (**B**) ROS levels in HepG2, Hep3B, and Huh7D-12 cells, 24, 48, and 72 h after incubation with Pd, Au, and Pd-Au NPs. ROS production was estimated using DHE. Results represent mean ± SD of three independent experiments. $^{***}P < 0.001$, $^{**}P < 0.01$, and $^{*}P < 0.05$ values are statistically significant in comparison to untreated control cells. $^{++}P < 0.01$ shows statistically significant difference observed between samples additionally preincubated with 5 mM NAC for 1 h. (**C**) HepG2, Hep3B, and Huh7D-12 cell viability was measured using Alamar Blue assay (resorufin assessments) after 48- and 72-h treatments of cells with varying concentrations of NPs in the absence or presence of free radical scavenger NAC (5 mM). Graphs show mean values ± SD from four independent experiments. $^{***}P < 0.001$, $^{**}P < 0.01$, and $^{*}P < 0.05$ for comparison with untreated control cells. $^{+++}P < 0.001$ and $^{++}P < 0.01$ for comparisons of cells preincubated with NAC (5 mM). (**D**) *CAT, SOD*, and *TXN* gene transcript expression relative to that of housekeeping genes in HepG2, Hep3B, and Huh7D-12 cells exposed to Au, Pd, and Pd-Au NPs for 48 h. $^{*}P < 0.05$, $^{**}P < 0.01$, and $^{***}P < 0.001$ for comparison of expression in cells treated with the investigated particles to that in untreated control cells.

was determined whether the intracellular concentration of reduced GSH was depleted (Figure 4C). Indeed, the GSH level remained unchanged in all examined human HCC cell lines treated with Au and Pd NPs. However, a 4-fold reduction in the GSH concentration was observed in Hep3B and Huh7D-12 cells and a 2-fold depletion was noted in HepG2 cells when the cells were incubated with Pd-Au NPs (60 µg/mL) for 48 h. This decrease was comparable to the GSH level observed in cells treated with a well-known GSH synthesis inhibitor, BSO, for up to 24 h.[58]

Along with the evaluation of intracellular GSH concentrations, the mRNA transcription levels of genes involved in GSH homeostasis were analyzed (Figure 4D). These included GSH peroxidase (*GPX*) and glutaredoxin (*GLRX*). The only alteration was observed in Huh7D-12 cells, showing a 0.75-fold downregulation of *GPX* in cells incubated with Pd-Au NPs.

Pd-Au NPs Induced Mitochondrial Dysfunction

Mitochondria play a central role in maintaining cellular energy homeostasis, regulating OS responses, and controlling cell fate decisions. Given their pivotal function, mitochondrial stress represents a key indicator of particle-induced cytotoxicity and may serve as a hallmark for assessing the antiproliferative potential of candidate compounds.[59,60] First, the dual-emissive fluorescent probe, JC-1, was used to evaluate mitochondrial membrane potential. High membrane potential leads to red fluorescence due to mitochondrial JC-1 aggregate formation, while low potential results in green

https://doi.org/10.2147/NSA.S589907

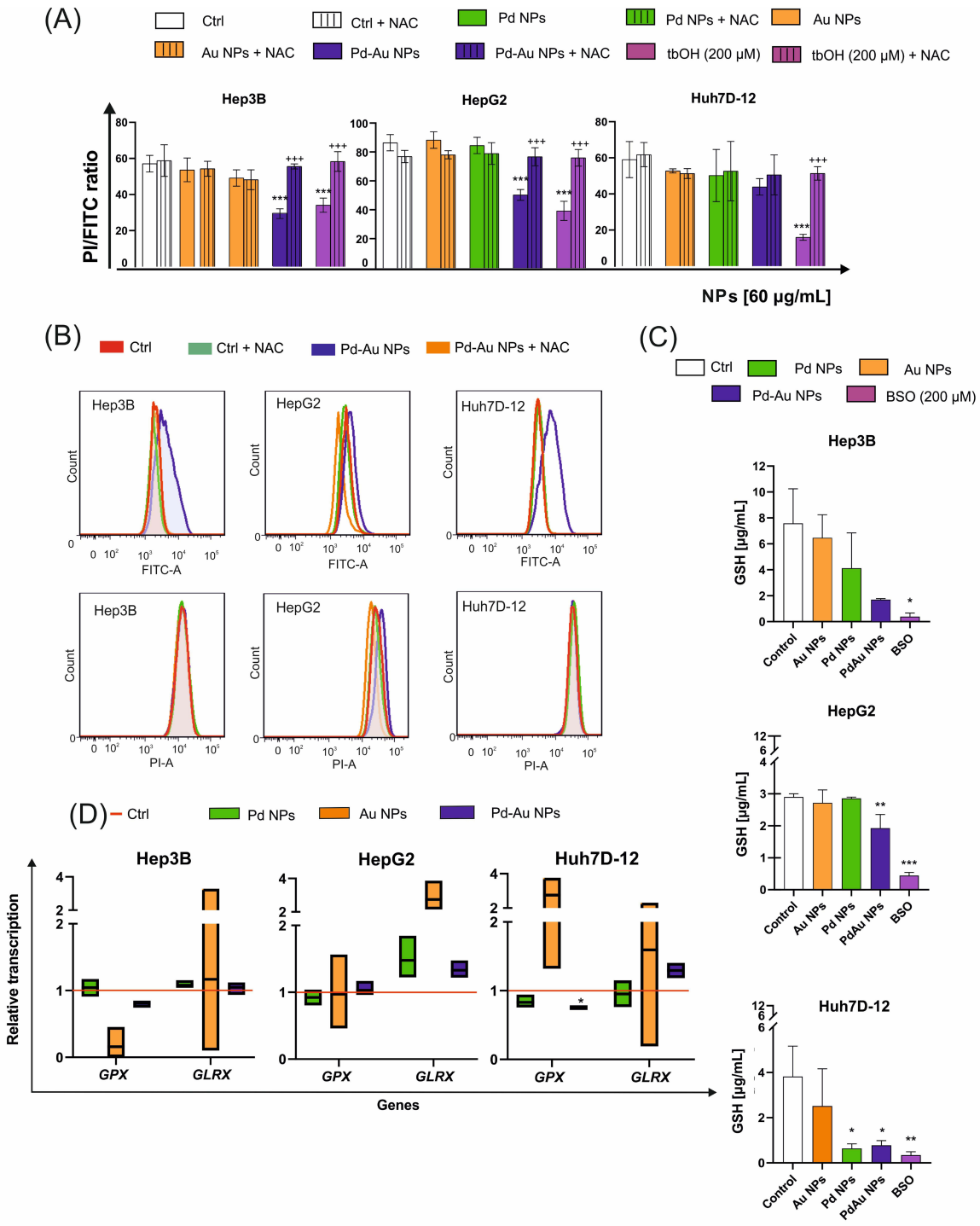

Figure 4 Oxidative stress markers in liver cancer cell lines exposed to Au, Pd, and Pd-Au NPs. (**A**) Changes in lipid peroxidation in HepG2, Hep3B, and Huh7D-12 cells following treatment with NPs (60 µg/mL) for 48 h at 37°C. Cells treated with tbOH (2 h, 200 µM) were used as a positive control. Bars (mean values ± SD from three independent experiments) represent the fold changes in reduced C_{11} BODIPY (red fluorescence) with reference to the oxidized probe C_{11} BODIPY (green fluorescence). ***$P < 0.001$ for comparison with data obtained in the absence of NPs. $^{+++}P < 0.001$ shows statistically significant difference between samples additionally preincubated with 5 mM NAC for 1 h. (**B**) Representative histograms for HepG2, Hep3B, and Huh7D-12 cells obtained during flow cytometry experiments after staining with C_{11} BODIPY for 30 min. C_{11} BODIPY was excited using a 488-nm argon laser and fluorescence was recorded on phycoerythrin (PE) and fluorescein isothiocyanate (FITC) detectors. (**C**) Effect of Au, Pd, and Pd-Au NPs on glutathione level (GSH concentration quantification was performed based on a prepared calibration curve). GSH synthesis inhibition by buthionine sulfoximine (BSO, 100 µM) for 24 h was used as a positive control for GSH depletion. *$P < 0.05$, **$P < 0.01$, and ***$P < 0.001$ for comparison with untreated control cells. (**D**) GSH-related mRNA transcription (*GPX* and *GLRX*) in the investigated HCC cell lines. Data are expressed as means ± SD of at least three distinct experiments, with *$P < 0.05$ showing significant differences from the respective controls.

https://doi.org/10.2147/NSA.S589907

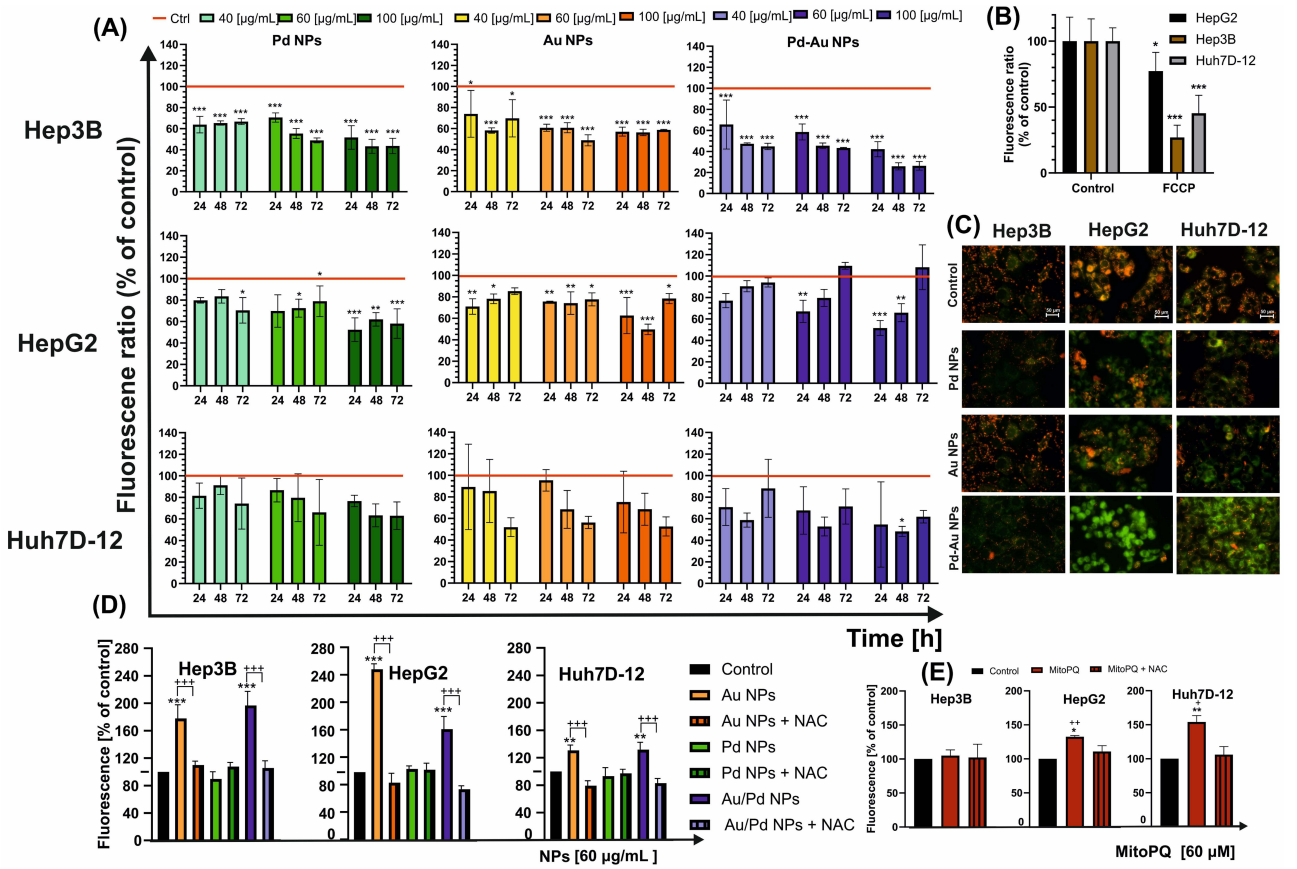

Figure 5 Disturbances in mitochondrial homeostasis triggered in HCC cell lines in vitro after their exposure to Au, Pd, and Pd-Au NPs. (**A**) Mitochondrial membrane potential (MMP) changes in examined cancer cells following 24-, 48-, and 72-h incubation with noble metal particles. Results are presented as fluorescence ratio of JC-1 dimers/JC-1 monomers of control cells, which was assumed to be 100%, and means ± SD of three independent experiments. Statistically significant changes are indicated in comparison with untreated cells taken as 100%; ***$P < 0.001$, **$P < 0.01$, and *$P < 0.05$. (**B**) Depletion of $\Delta\Psi$ triggered by FCCP (100 µM, 4 h) was used as a positive control for MMP alteration; ***$P < 0.001$ and *$P < 0.05$ show significant differences between control (taken as 100%) and FCCP-treated cells. (**C**) Fluorescence microscopy images of hepatocarcinoma control cells and cells treated with NPs for 48 h. A decrease in the red-to-green fluorescence intensity ratio is a direct indicator of mitochondrial membrane depolarization. JC-1-stained cells were visualized under an inverted fluorescence microscope (Olympus IX70, Japan), 400 x magnification. Scale bar 50 µm. (**D**) Mitochondrial ROS generation in HepG2, Hep3B, and Huh7D-12 cells after treatment with examined NPs was measured after 48 h in the presence or absence of NAC. Control cells were assumed to indicate 100%. ***$P < 0.001$, **$P < 0.01$ for comparison with data obtained in the absence of NPs, $^{+++}P < 0.001$ for comparison with cells preincubated with NAC. (**E**) Positive control cells (for mitochondrial ROS production) were treated with MitoPQ (10 µM) for 24 h. Data are expressed as mean ± SD of at least three experiments. Statistically significant changes between samples incubated with tested compounds compared to control cells (**$P < 0.01$, *$P < 0.05$). Statistically significant changes between samples incubated with NPs and those preincubated with NAC ($^{++}P < 0.01$, $^{+}P < 0.05$).

fluorescence from cytosolic JC-1 monomers. Mitochondrial dysfunction indicated by a decreased membrane potential was assessed based on the reduced ratio of red-to-green fluorescence intensity. All investigated NPs triggered the loss of Δψm in a time- and concentration-dependent manner (Figure 5A). A decrease in JC-1 fluorescence intensity was comparable for Hep3B and HepG2 cancer cells treated with Pd and Pd-Au NPs. However, the most significant drop in mitochondrial membrane potential (MMP) level was observed in Hep3B cells, which decreased by nearly 25% compared to the control value after 48 h of incubation with Pd-Au NPs. Importantly, MMP hyperpolarization was observed when the incubation with the same type of particles was prolonged to 72 h, but only in HepG2 cells. A fall in MMP level was also noted when the cells were incubated with the positive control. FCCP (4 h, 100 µg/mL), which reflected a decrease in the JC-1 dimer to JC-1 monomer fluorescence ratio as follows: Hep3B > Huh7D-12 > HepG2 (Figure 5B). Additionally, Δψm in the NP-treated cells was monitored using fluorescence microscopy. The Pd-Au NP treatment caused an increase in green fluorescence of JC-1 monomers in liver cancer cells, indicating a reduction in MMP level (Figure 5C). In contrast, the red fluorescence of JC-1 dimers was seen in untreated (control) cells with a high MMP level.

The differential alterations in MMP and OS marker levels that appeared after the treatment of liver cancer cells with the investigated NPs warranted an assessment of whether mitochondria could be the crucial cellular compartment where

https://doi.org/10.2147/NSA.S589907

ROS production takes place in these experimental conditions. Thus, the level of free radicals was evaluated using the MitoSOX assay, and the measurement of ROS generation was reserved only for mitochondria (Figure 5D). Because the most significant depletion of MMP was recorded after 48 h of incubation with NPs (60 µg/mL), the prime source of mitochondrial ROS was determined to be not only Pd-Au NPs (2-fold increase in Hep3B cells) but also Au NPs (2.5-fold growth in HepG2 cells). Half of the tested samples were pretreated with NAC to confirm that the observed signal was a ROS-specific consequence and not an unrelated cellular response. Additionally, the reliability of this assay was confirmed by a 4-h incubation of cells with MitoPQ (Figure 5E), which selectively increased superoxide production within mitochondria (primarily in HepG2 and Huh7D12 cells) through redox cycling at the flavin site of complex I.

As ROS production and the changes in MMP level are the commonly known molecular markers for mitochondrial stress, the MITOTOX assay was performed to evaluate the ATP content and assess mitochondrial membrane integrity (Figure 6A and B). The two parameters were analyzed with a reference to HCC cells treated with FCCP (100 µM, 4 h), which served as a positive control. Among the tested particles, only Pd-Au NPs (60 µg/mL) caused an approximately 2-fold reduction in the intracellular ATP level in Hep3B, HepG2, and Huh-7D12 cells following a 48-h incubation (Figure 6A). These alterations corresponded with the mitochondrial membrane damage (Figure 6B) triggered by the core-shells, resulting in a 2.3-fold increase in the fluorescence signal in HepG2 cells. The global visualization and quantification (Figure 6C) of mitochondrial homeostasis was carried out using MitoTracker deep red staining (Figure 7). Measuring the fluorescence intensity of HCC cells labeled with MitoTracker deep red revealed that all investigated NPs caused a concentration-dependent mitochondrial homeostasis perturbation. A 3-fold decrease in the signal of Mito Tracker Deep Red-labelled HepG2 and Hep3B cells was noted following a 48-h incubation with Pd-Au NPs (100 µg/mL). Consistent with these changes, the transcription of the *Bax* and *Bcl-2* genes, which are involved in the

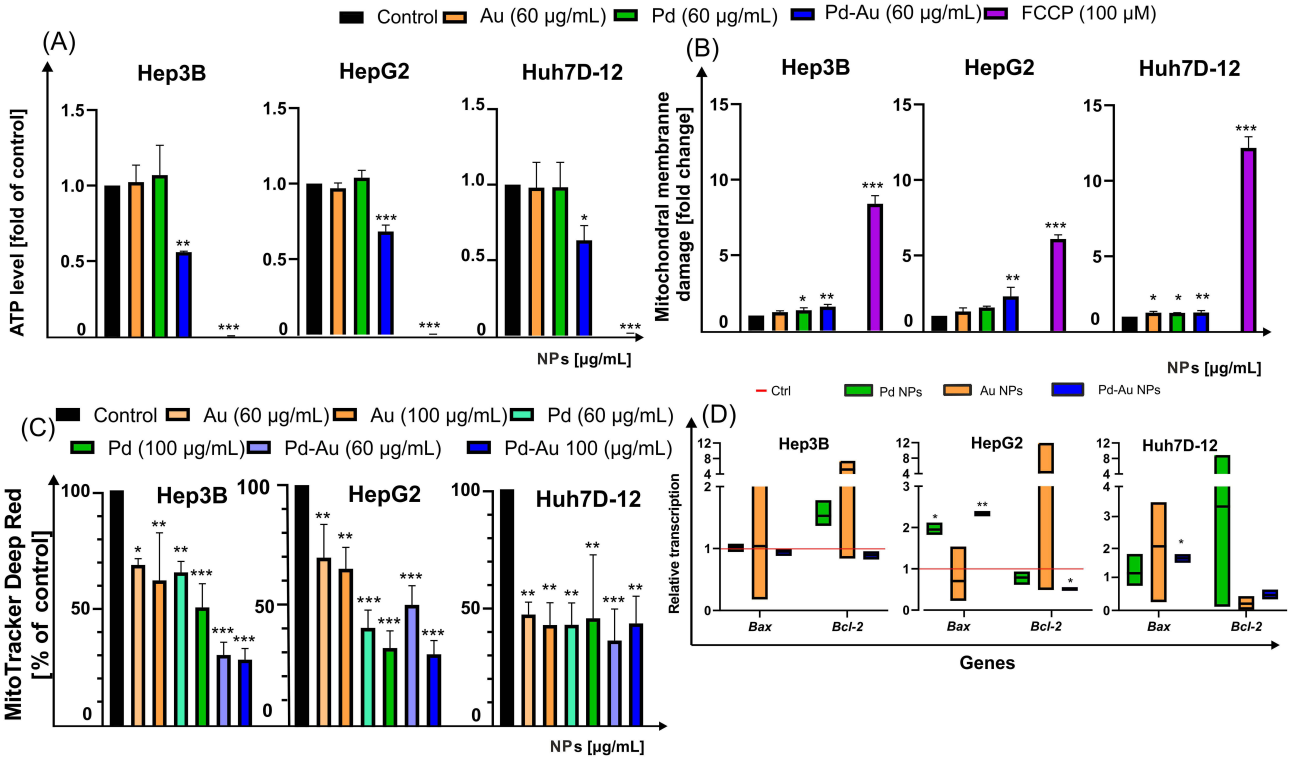

Figure 6 Mitochondrial stress induced by Au, Pd, and Pd-Au NPs in human hepatocarcinoma in vitro cultures. (**A** and **B**) Mitochondrial toxicity of examined noble metal NPs (60 µg/mL) toward HepG2, Hep3B, and Huh7D-12 cells after 48 h of treatment. Measurement included evaluation of (**A**) ATP level and (**B**) mitochondrial membrane integrity. Incubation of cells with FCCP (100 µM, 4 h) was used as a positive control; ***$P < 0.001$, **$P < 0.01$, and *$P < 0.05$ for comparison with data obtained in the absence of NPs. (**C**) Measurements of MitoTracker deep red fluorescence after 48-h incubation at 37°C in HepG2, Hep3B, and Huh7-D12 cells with 60 µg/mL of NPs. Median fluorescence intensity of MitoTracker deep red was quantified in at least five different images. Error bars show mean ± SD from three independent experiments. Statistically significant changes between samples incubated with tested compounds compared to control cells (***$P < 0.001$, **$P < 0.01$, and *$P < 0.05$). (**D**) Transcription of *Bax* and *Bcl-2* mRNA in HepG2, Hep3B, and Huh7D-12 cells treated with Au, Pd, and Pd-Au NPs for up to 48 h. Asterisks refer to expression differences in cells treated with tested compounds compared to those in untreated cells (*$P < 0.05$, **$P < 0.01$).

https://doi.org/10.2147/NSA.S589907

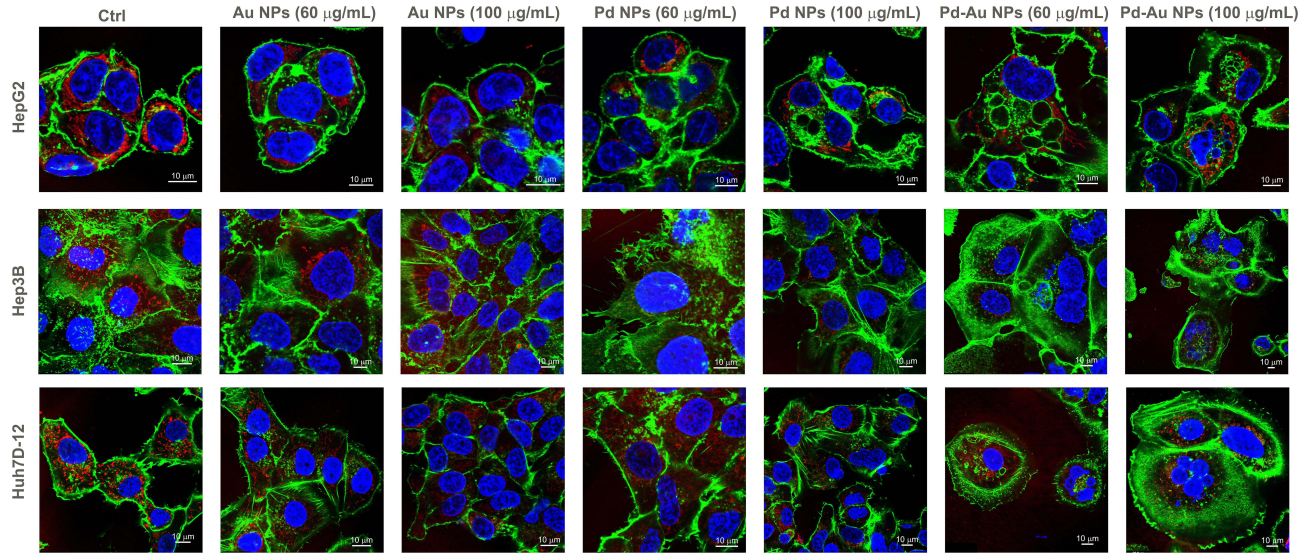

Figure 7 Representative fluorescence micrographs of HepG2, Hep3B, and Huh7D-12 cells treated with Au, Pd, and Pd-Au NPs. Images obtained during confocal microscopy analyses show the maximum intensity projection of the investigated in vitro HCC cultures treated with 60 μg/mL of the examined particles for 48 h. The study was performed three times, with 10–15 cells analyzed per experiment. Cell nuclei were stained with DAPI (blue), mitochondria were stained with MitoTracker deep red (red), and F-actin filaments were stained with phalloidin Alexa Fluor 488 (green). Scale bar represents 10 μm.

mitochondria-dependent pathways of cell death, was assessed (Figure 6D). Both Pd and Pd-Au NPs induced a comparable ~2-fold increase in *Bax* transcription in HepG2 cells, whereas Pd-Au core-shells triggered a 1.7-fold rise in *Bax* mRNA levels in Huh 7D-12 cells. Additionally, an approximately 2-fold downregulation of *Bcl-2* transcription was observed in HepG2 cells treated with Pd-Au NPs. In contrast, no change in *Bax* or *Bcl-2* transcription was detected in Hep3B cells.

Neither Pd NPs nor Pd-Au NPs Induced Apoptotic Cell Death

Given the differential effects of Pd-based NPs on ROS production, OS, and mitochondrial stability, the mode of cell death induced by the three tested types of NP variants was then identified. The cells were exposed to the examined NPs (60 μg/mL) for up to 48 h of continuous incubation. In parallel with MitoTracker deep red staining, phalloidin and DAPI dyes were used to track the organization of actin filaments and follow the alterations in nuclear morphology, respectively (Figure 7). The apoptosis induction was thus briefly assessed. However, exposure to either Pd or Au NPs in the examined hepatoma cell lines did not elicit classical apoptotic features, such as pronounced membrane blebbing or cellular shrinkage. Instead, the predominant morphological responses included cell rounding, detachment, swelling, and rupturing. Apoptosis-like characteristics were noticed only sporadically, suggesting that these particles primarily induced non-apoptotic forms of cell death. The Annexin V Apoptosis and Necrosis kit, a well-established apoptosis assay, was further used to evaluate apoptosis induction.[61] Notably, Pd-Au NPs induced an increase in the luminescence signal (here reserved for apoptosis) in all examined cell lines, with a nearly 6-fold increase in the number of Annexin V-positive cells observed in Huh7D-12 cells (Figure 8A). This, however, did not align with the sample preincubated with z-VAD, an inhibitor of apoptosis and caspase-3. Only HepG2 cells showed a 2-fold difference between samples exposed to Pd-Au NPs with or without z-VAD pretreatment. This was in agreement with the higher expression of *Bax* and downregulation of *Bcl-2* transcription (Figure 6D) observed only in Pd-Au NP-treated cells. In contrast to Pd-Au NPs, Pd and Au NPs generally promoted a lower population of cells with phosphatidylserine externalization. Consistent with the luminescence measurement of apoptosis, the necroptosis level was analyzed using a fluorometric assessment of cell membrane rupture. Importantly, all examined cell lines treated with Pd-Au NPs showed an elevated necroptosis signal. Consistent with their enhanced cytotoxicity, Pd-Au bimetallic NPs induced pronounced cytoskeletal disruption, as evidenced by phalloidin staining and confocal microscopy results (Figure 7). This suggested that Pd-Au core-shells triggered another type of nonapoptotic, regulated cell death. Caspase-3/7 activation was measured to further investigate the NP-selective cell death

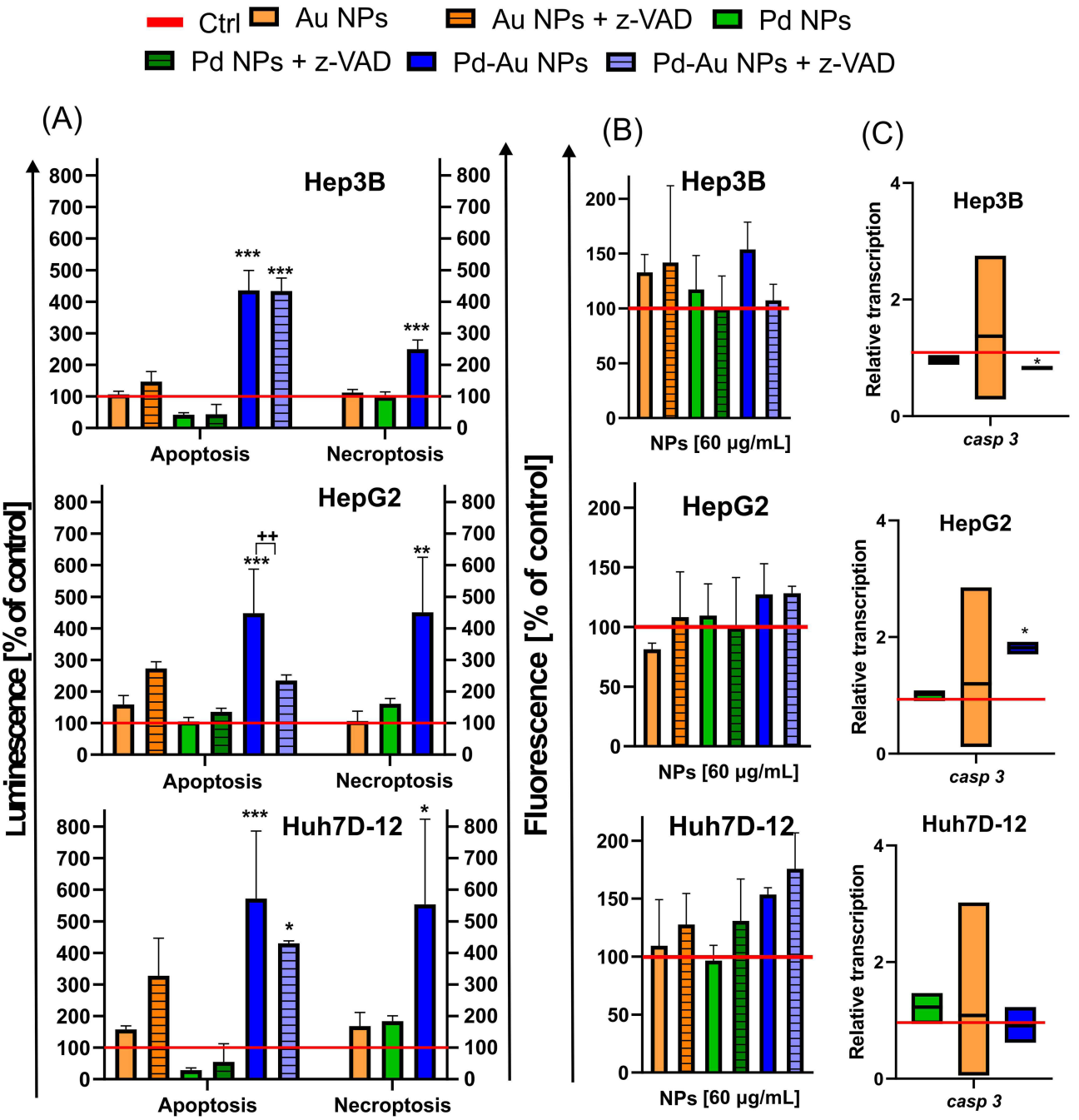

Figure 8 Apoptosis assessment in HCC cells in vitro incubated with Au, Pd, and Pd-Au NPs. (**A**) Externalization of PS (phosphatidylserine) in human HCC cells treated with examined NPs (100 µg/mL) for up to 48 h. Data are shown as mean of percentages ± SD of annexin-V-binding cells (left panel) and cells with cellular membrane damage (right panel) from three independent experiments. Additional incubation with caspase-3 inhibitor z-VAD (20 µM) was performed in samples identified by a high Annexin-V signal; ***$P < 0.001$, **$P < 0.01$, and *$P < 0.05$ indicate significant differences between particle-treated and control cells; $^{++}P < 0.01$ shows differences between samples pretreated with z-VAD. (**B**) Changes in caspase-3/7 activity in HepG2, Hep3B, and Huh7D-12 cells treated with NPs (60 µg/mL) for up to 48 h. Measurements were carried out in the presence or absence of z-VAD. Results represent means ± SD of three independent experiments. **(C)** *Casp-3* transcription level (relative to *HPRT1* and *HMBS*) in HCC cell lines exposed to NPs (60 µg/mL) for 48 h. Asterisks refer to significant differences (*$P < 0.05$, n = 3) in transcription levels in NP-treated cells compared to those in untreated cells.

modes (Figure 8B). Even though the fluorescence signal of the CellEvent Caspase-3/7 substrate increased in HCC cell lines treated with Pd-Au NPs, these changes were at the same level as those in samples preincubated with zVAD. Monitoring the *casp-3* mRNA levels revealed a 1.8-fold increase in caspase-3 transcription exclusively in HepG2 cells treated with core-shells (Figure 8C). The same treatment conditions in Hep3B cells caused a decrease in *casp-3*

 https://doi.org/10.2147/NSA.S589907

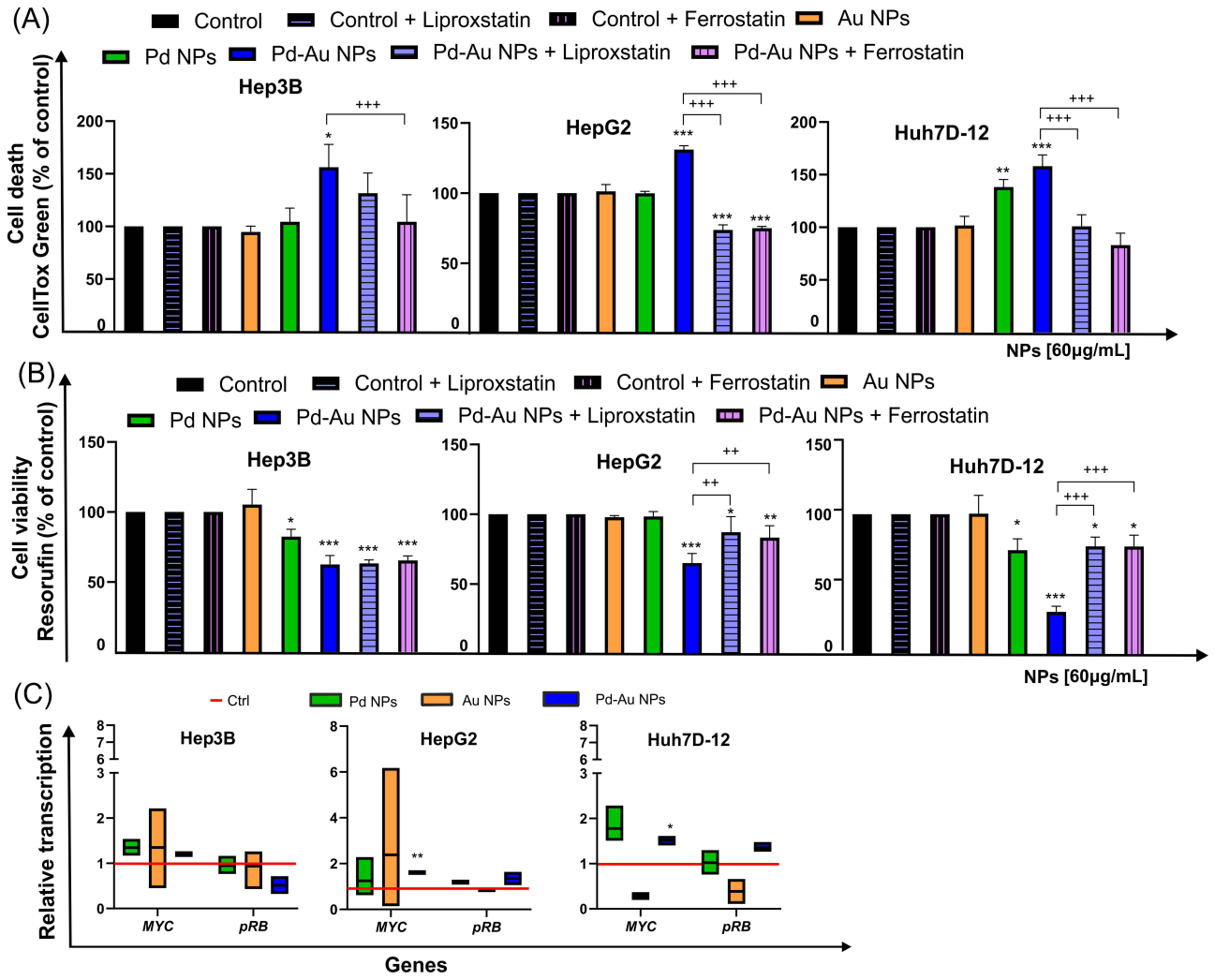

Figure 9 Pd-Au NPs induce ferroptosis in HCC cell lines. (**A**) Quantification of cell death (CellTox Green) in HepG2, Hep3B, and Huh7D-12 cells treated with Au, Pd, and Pd-Au NPs (100 µg/mL) in the presence or absence of liproxstatin-1 (Lipro, 1 µM) or ferrostatin (Ferro, 2 µM). Each replicate (n = 3) is from a single biological experiment and quantified using three independent wells. Graphs show mean values ± SD from three independent experiments. **P* < 0.05, ***P* < 0.01, and ****P* < 0.001 for comparison of untreated control cells; ^{+++}P < 0.001 for comparison of cells treated with Lipro or Ferro. (**B**) Ferroptosis inhibitors protect HepG2 and Hep3B cells, but not Huh7D-12 cells from Pd-Au NP-induced toxicity. Cytotoxicity was assessed by measuring resorufin levels (Alamar Blue assay) in HCC in vitro cultures treated with varying concentrations of examined NPs in the presence or absence of Lipro (1 µM) or Ferro (2 µM). Data are shown as a percentage of control for each cell line not treated with Pd or Pd-Au NPs. **P* < 0.05, ***P* < 0.01, and ****P* < 0.001 for comparison with data obtained in the absence of examined particles. ++*P* < 0.01, +++*P* < 0.001 for comparison of cells preincubated with Lipro or Ferro. (**C**) *MYC* and *pRB* transcription levels relative to housekeeping genes *HPRT1* and *HMBS* in HepG2, Hep3B, and Huh7D-12 cells exposed to Au, Pd, and Pd-Au NPs (60 µg/mL) for 48 h. Asterisks refer to significant differences (**P* < 0.05, ***P* < 0.01; n = 3) in expression levels in cells treated with NPs compared to untreated cells.

transcription level. In contrast, no change in *casp-3* mRNA levels was detected in Huh7D-12 cells following incubation with the examined particles. Thus, it was speculated that apoptosis was not the predominant type of regulated cell death triggered by Pd-Au core-shells.

Pd-Au NP-Induced Death Occurred by Ferroptosis

Based on the assay results described above, the mechanism of ROS-dependent cell death triggered by Pd-Au NPs with core-shell structures was then characterized. Detailed morphological analysis of the dying cells revealed features consistent with a necroptotic phenotype (Figure 7). A panel of methods that excluded the apoptotic form of cell death was used to more definitively identify the cell death mechanism. First, all examined cells displayed a downregulation of *Bax* and *casp-3* transcription in parallel with *Bcl-2* overexpression (Figure 6D). In addition, neither annexin V-positive cells nor caspase-3 activation happened when hepatocarcinoma cells were treated with Pd-Au NPs. Next, it was

https://doi.org/10.2147/NSA.S589907

determined whether ferroptosis, a cell death mechanism that occurs via an iron and lipid ROS-dependent process and is induced by GSH depletion, was involved in Pd-Au NP-induced cell death. The abovementioned molecular markers were noted in Hep3B and HepG2 cells. It was also determined whether Ferro and Lipro, pharmacological inhibitors of ferroptosis that are scavengers of lipid ROS, blocked cell death in this context. Thus, the CellTox Green assay (Figure 9A) was performed on Hep3B, HepG2, and Huh7D-12 cells exposed to Pd-Au, Pd, and Au NPs for up to 48 h. Treatment with both tested inhibitors restored cell viability, reducing cell mortality to the level observed in the absence of Pd-Au core-shells. Pd-Au NP-triggered reduction of viability was also inhibited by the treatment with Ferro and Lipro in HepG2 and Huh7D-12 cells (Figure 9B), as well as another antioxidant NAC, which is a precursor of GSH (Figure 3C). This phenomenon was noted only in cells incubated with Pd-Au NPs (60 µg/mL) for up to 48 h. Consistent with the toxicity assays performed in combination with ferroptosis inhibitors, the transcription of *pRB* and *MYC* (Figure 9C) involved in iron-dependent cell death was analyzed.[62,63] Importantly, an approximately 1.5-fold increase in *MYC* mRNA levels in HepG2 and Huh7D-12 cells treated with Pd-Au NPs was demonstrated. Neither Pd NPs nor Pd-Au NPs altered pRB mRNA levels in any of the HCC cell lines.

Discussion

Despite significant progress in liver cancer therapy, such as targeted and immunotherapies, liver transplantation is still the most efficient option to prolong the quality of life in patients with HCC. Apart from this procedure, surgical tumor resection, transarterial chemoembolization, radioembolization, and the use of broad-spectrum tyrosine kinase inhibitors are the approved treatments for advanced HCC.[64,65] These strategies provide a nominal extension of the survival curve. Still, these improvements are measured in months and result in broad-spectrum toxic side effects, ultimately leading to patients developing resistance to therapy. Therefore, NP-based therapies have been developed, and the applications of ultra-small particles are being extensively investigated against aggressive and fast-growing cancers, such as HCC.

The present study demonstrated that differences in the structure of noble metal-based NPs designed explicitly for translational medicine dictated their interaction with hepatoma cancer cells and cell death mode. Even though Au NPs induced mitochondrial ROS and triggered some mitochondrial disturbances, they did not diminish the viability of either of the examined hepatocellular cell lines. However, Pd NPs displayed a decrease in all examined cell survivals, although the generation of free radicals was triggered only in HepG2 cells. Thus, it could not be confirmed whether ROS production was the trigger for mitochondrial stress induction or the primary cytotoxicity mechanism for these particles, because a well-known antioxidant NAC did not protect the cells treated with Pd NPs. Furthermore, Pd-Au NP experiments demonstrated that a substantial reduction in HCC viability was attributed to the generation of ROS, mitochondrial stress, and ferroptosis induction. These effects were reversible with NAC, Lipro, and Ferro but not with zVAD (Table 4).

It is well established that Pd-based nanomaterials have numerous biomedical applications.[66] As a therapeutic and gene-loading nanosystem, Pd nanoplates can provide a gene-thermal combinational cancer therapy in vitro.[67] Additionally, Pd NPs serve as drug delivery vehicles for anticancer radioisotopes, such as ^{131}I, used in radiotherapy,

Table 4 Summary of the Direction and Statistical Significance of Biological Responses Induced by Au, Pd and Pd-Au NPs

NP Type	Cytotoxicity		Oxidative Stress	Mitochondrial Stress	Apoptosis	Necroptosis	Ferroptosis
	AB	MTT					
Au	—	—	—	↓↓	—	—	—
Pd	↑↑	↑	—	↓↓↓	—	↑↑	—
Au–Pd	↑↑↑	↑↑↑	↑↑↑	↓↓↓	—	—	↑↑↑

Notes: Arrows indicate the direction of change relative to the control, and the number of arrows reflects the level of statistical significance (↑$P < 0.05$, increase; ↑↑$P < 0.01$, increase; ↑↑↑$P < 0.001$, increase; ↓$P < 0.05$, decrease; ↓↓$P < 0.01$, decrease; ↓↓↓$P < 0.001$, decrease). Symbol "—" denotes no statistically significant effect.

or chemotherapeutic agents, eg, doxorubicin.[68] Functionalized with precise ligands, Pd NPs transport therapeutic agents that disrupt irregular DNA replication and protein synthesis, potentially limiting the abnormal cancer cell proliferation.[69,70]

The NP size measurement is one of the first steps in the evaluation of physicochemical nanomaterial properties used for biomedical applications. The comparison of Pd, Au, and Pd-Au NP diameters estimated using DLS or TEM (Figure 1) revealed some discrepancies. The data obtained from DLS measurements showed that the particles could be 25 times larger (Pd NPs) than those indicated in the data gained during TEM analyses. However, this disagreement is quite common and stems from the fundamental principles behind each technique. TEM measurements exclude any surface coatings, solvent layers, or agglomerates unless explicitly visible.[71] DLS measures the size of NPs together with NP aggregates, clusters, solvent molecules tightly bound to their surface, and surface stabilizers, which are not visible in TEM.[72] This is especially relevant for Au NPs, which were stabilized with citrate, in the present study. Furthermore, the high standard deviations in DLS (especially for Au and Pd NPs) indicated broad size distributions. This occurred because the DLS technique was intensity-weighted, and larger particles dominated the signal.[73]

The NP size is the second important property that plays a crucial role during their intracellular uptake. In this report, all tested NPs displayed a slightly negative ζ-potential (below −15 mV). Numerous studies have shown that positively charged NPs are internalized more efficiently by cells.[74–76] Because particles with a positive charge will bind to the negatively charged cell surface, it is expected that positively charged particles are taken up more efficiently than negatively charged particles. A study in HeLa cells with positively and negatively charged NPs of equal size (80 nm) showed a 2-fold higher uptake of the positively charged particles.[77] In contrast, a higher uptake of negatively charged NPs has been reported in HEK cells.[78] Thus, some studies indicate no clear relationship between NP surface charge and the rate of intracellular transport, indicating that NP uptake cannot be reliably predicted based on surface charge alone.

Generally, when NPs enter cells, they produce cytotoxic effects. Consequently, different types of cellular disturbances are activated, resulting in a reduction of cellular viability and proliferation.[79–81] Alkhalidi et al reported that green synthesis of acid protease-mediated Pd NPs inhibited the proliferation of MCF-7 cells with an IC_{50} of 66.37 μg/mL.[82] In addition, cytotoxic effects of Pd NPs on MDA-MB-231, HepG2, and HeLa cells were observed by Shivakumar et al, reporting 70%, 50%, and 60% reductions in cell viability, respectively.[83] Pd-based nanosystems do not always act on their own; a synergistic effect of Pd NPs and a selective HDAC6 inhibitor tubastatin A was described in a study by Yuan et al[84] Combining these two agents significantly reduced the cell viability of MDA-MB-231 human breast cancer cells by up to 70%, whereas tubastatin A or Pd NPs alone achieved only a 25% reduction.

In the present study, Pd-Au bimetallic NPs showed the strongest cytotoxic effects across all applied assays, including intracellular reductase activity (MTT, Alamar Blue), cellular ATP levels (CellTiter-Glo), and membrane integrity (CellTox Green). This consistent pattern suggested that the increased toxicity of Pd-based core-shells reflected a genuine biological effect rather than assay-specific effects. Additionally, the calculated IC_{50} (around 60 μg/mL) for these particles reached similar values for all three investigated cell lines (Figure 2 and Table 3). Neither Au NPs nor Pd NPs displayed such a robust effect toward HCC cell survival. The most widely accepted mechanism underlying NP-induced cytotoxicity involved a surge in ROS, which disrupted cellular homeostasis by damaging key biomolecules, including nucleic acids, proteins, lipids, and carbohydrates, ultimately impairing essential physiological functions.[24] Several studies have suggested that various types of NPs induce cytotoxicity in cancer cells by producing ROS, which, in turn, leads to cellular damage and cell death.[84–86]

It has been postulated that Pd nanomaterials show exceptional catalytic activity due to their ROS overproducing effects. This property prioritizes the use of these compounds over other NPs, such as Au or Ag NPs.[68,87] Thapa et al used Pd NP-decorated graphene oxide (GO-Pd NPs) in combination with near-infrared light to treat a solid prostate cancer tumor in a murine model, observing that intratumorally administered GO-Pd NPs exerted a high photothermal effect, perhaps via ROS generation.[88]

Conversely, a dramatic increase in ROS production triggered solely by Pd NPs (apart from HepG2 cells after 48 h of incubation with NPs) was not observed in the present study. On the contrary, treating all examined HCC cells only with Pd-Au NPs resulted in ROS generation, which NAC effectively diminished. The predominant role in triggering ROS in cells, such as by lipid peroxidation, GSH depletion, or altered transcription of antioxidative enzymes, was also attributed

to Pd-Au core-shells but not to Pd NPs (Figures 3 and 4). A reduction in GSH level (1.13-fold) was recorded in HepG2 cells treated with Pt-Au NPs.[89] In contrast to the present study data, Gurunathan et al demonstrated that SKOV-3 ovarian cells exposed to Pd NPs exhibit a dose-dependent decrease in the levels of antioxidants, such as GSH, and in SOD enzyme activity.[90] In line with this reduction, the same group observed that Pd NPs caused an increase in malondialdehyde content, a well-known marker of lipid peroxidation, and ROS overproduction, as monitored with the DCFH-DA (2',7'-dichlorodihydrofluorescein diacetate) probe. A significant difference in the response of the examined cell lines was observed when evaluating the role of oxidative and mitochondrial stress in Pd-based particle cytotoxicity. The reasons for this diverse reaction were further explored.

First, the HCC cell lines used in the present study originated from different liver cancer tissues and exhibited varying levels of tumorigenicity. These alterations were partly related to the expression of the p53 protein, whose mutated form (p53 Y220C) is expressed in Huh7D-12 cells.[91] Because p53 plays a key role in regulating oxidative stress responses and mitochondrial integrity, it may impair the ability of the cell to undergo ROS-induced cell death. Second, HepG2 and Hep3B cells exhibited higher mitochondrial respiration and ATP production compared to Huh7D-12 cells, which may be why these cells were less responsive to ROS-induced cytotoxicity.[92] Huh7-D12 cells express high levels of antioxidant enzymes (eg, GSH S-transferase, catalase) necessary for maintaining proper oxidative homeostasis.[93] Third, the diverse metabolic rates of the HCC cells could be due to their viral susceptibility. Huh7D12 cells are highly permissive to the HCV,[94] whereas Hep 3B cells have a naturally integrated HBV genome within their DNA.[95] Even though HepG2 cells do not naturally contain HBV DNA, this cell line is often used in HBV-dependent transcription and replication studies.[96]

When exploring the cytotoxic consequences of ROS production and regulated cell death induction, the oxidative damage caused by Pd-Au NPs and the resulting mitochondrial effects may be contributing factors for cellular fatality. The potential of Pd NPs to induce mitochondrial damage was first reported by Gurunathan et al,[97] who demonstrated that in vitro co-treatment of lung cancer cell lines A549 or H1229 with melatonin exacerbated mitochondrial dysfunction. This was evidenced by a reduction in MMP, ATP levels, and mitochondrial number, along with altered expression of key mitochondrial biogenesis regulators.

In the present study, only Pd-Au NPs exhibited pronounced mitotoxic effects, initially observed through confocal microscopy as significant disruptions in mitochondrial structure. This was subsequently confirmed by a marked decrease in mitochondrial membrane potential, ATP level depletion, increased mitochondrial ROS production, and structural damage to the mitochondrial membrane (Figures 5–7). The results of qRT-PCR analysis of *Bax* and *Bcl-2* transcription may suggest the induction of apoptosis during incubation of HCC cells with Pd-Au NPs.

However, apoptosis was not the primary type of cell death induced in this case (Figure 8), as a protective effect with zVAD was not observed either in the annexin detection assay or during caspase-3/7 activation assessment. The data contradicted the results reported by Ramalingam et al,[20] where PVP-Pd NPs induced apoptosis in MCF-7 cells with a lower IC_{50} than cisplatin and free oxalipalladium. The MCF-7 cells also exhibited a high susceptibility to Pd NPs, which triggered the phosphatidylserine externalization, cell membrane disintegration, and chromosome condensation.[98] Furthermore, Pd/MgO NPs stimulated caspase-3 and −9 activation, together with a decrease in Bcl-2, an increase in Bax protein level, and cytochrome c release in HT-29 and A549 cells.[99]

Pd-Au NPs triggered ferroptosis in HCC cell lines (Figure 9). This discovery was confirmed using ferroptosis inhibitors, Lipro and Ferro, which increased HCC cell survival as measured by the Alamar Blue assay, and diminished the Pd-Au NP-induced cytotoxicity as evaluated with the CellTox Green assay. Furthermore, transcriptional analysis of *MYC* revealed its upregulation exclusively in HCC cells treated with Pd-Au core–shell particles.

A key question raised by these findings is why only these particles induce ferroptosis and how it relates to their robust cytotoxicity? The fact that only Pd-Au core-shells trigger ferroptosis in HCC cell lines, while Pd NPs and Au NPs alone do not, suggests that the core-shell architecture plays a critical role in the initiation of this specific form of cell death.

A key question raised by these findings is why do only these particles induce ferroptosis and how does it relate to their robust cytotoxicity? The fact that only Pd-Au core-shells triggered ferroptosis in HCC cell lines, while Pd and Au NPs alone did not, suggested that the core-shell architecture played a critical role in the initiation of this specific form of cell death.

The Au NP surface can be easily functionalized with targeting ligands or other metals,[100] which enhances their selective uptake by cancer cells and facilitates other anticancer applications, such as synergistic therapies involving Auger electrons.[30] Additionally, the Au core of Au NPs contributes to their high biocompatibility and oxidation resistance.[101] The present data demonstrated that Pd-Au core-shells exhibited properties that facilitated ROS generation. It has recently been proposed that Pd-Au NPs behave as nanozymes, mimicking the activity of peroxidase. These NPs catalyze the conversion of excess H_2O_2 in the tumor microenvironment and disrupted redox homeostasis of cancer cells.[102] Finally, surface plasmon resonance analyses of different types of core-shell NPs, showed enhanced electron transfer reactions at the NP surface and promoted Fenton-like reactions, leading to ROS generation and oxidative stress.[103]

Conclusion

In summary, the present study demonstrated that Pd-based NPs exhibited distinct mechanisms of promoting cytotoxicity and cell death pathways (Table 4). Ultra-small Pd NPs had a moderate effect on in vitro HCC cell viability and proliferation and promoted necrosis. However, cytotoxic Pd-Au core-shells displayed a dual mechanism of direct ROS generation and ferroptosis promotion. Their ability to induce lipid peroxidation, GSH depletion, and alteration of the transcription of several antioxidant proteins in human liver cancer cells highlighted their potential as promising nanoagents against tumors with disturbed redox homeostasis. By better understanding their underlying molecular mechanisms, NPs can be optimized for individual clinical applications and thus provide higher efficacy, and better therapeutic potential against HCC and possibly other tumors.

In summary, the present study demonstrated substantial differences (physical, toxicological, and biological) among the three NPs studied in human liver tumor cells. Pd-based NPs exhibited distinct mechanisms of promoting cytotoxicity and cell death. Ultra-small Pd NPs had a moderate effect on in vitro HCC cell viability and proliferation and promoted necroptosis. In contrast, Pd-Au core-shells displayed more biological activity, including more toxicity, direct promotion of ROS generation, and increased ferroptosis promotion. The ability of the Pd-Au NPs to provoke lipid peroxidation, GSH depletion, and alteration of the transcription of several antioxidant proteins in human liver cancer cells highlighted their potential as a promising nanomaterial useful against tumors by disturbing redox homeostasis. Understanding of the underlying molecular mechanisms of Pd-Au NPs will be pivotal in unlocking their full therapeutic potential against human tumors.

Disclosure

The authors report no conflicts of interest in this work.

References

1. Llovet JM, Kelley RK, Villanueva A, et al. Hepatocellular carcinoma. *Nat Rev Dis Primers*. 2021;7(1):6. doi:10.1038/s41572-020-00240-3
2. Suresh D, Srinivas AN, Prashant A, Harikumar KB, Kumar DP. Therapeutic options in hepatocellular carcinoma: a comprehensive review. *Clin Exp Med*. 2023;23(6):1901–1916. doi:10.1007/s10238-023-01014-3
3. Jardim SR, de Souza LMP, de Souza HSP. The rise of gastrointestinal cancers as a global phenomenon: unhealthy behavior or progress? *Int J Environ Res Public Health*. 2023;20(4):3640. doi:10.3390/ijerph20043640
4. Li MM, Yuan J, Guan XY, Ma NF, Liu M. Molecular subclassification of gastrointestinal cancers based on cancer stem cell traits. *Exp Hematol Oncol*. 2021;10(1):53. doi:10.1186/s40164-021-00246-x
5. Deyirmendjian C, Padda B, Fowler KJ, et al. Prognostic and predictive imaging markers of hepatocellular carcinoma: a pictorial essay. *Insights Imaging*. 2025;16(1):181. doi:10.1186/s13244-025-02058-7
6. Vogel A, Meyer T, Sapisochin G, Salem R, Saborowski A. Hepatocellular carcinoma. *Lancet*. 2022;400(10360):1345–1362. doi:10.1016/S0140-6736(22)01200-4
7. Li X, Chen K, Feng X, et al. A comparative study of surgical approaches for hepatocellular carcinoma: conversion versus direct resection. *J Hepatocell Carcinoma*. 2024;11:2101–2113. doi:10.2147/JHC.S483397
8. Armakolas A, Dimopoulou V, Nezos A, et al. Cellular, molecular and proteomic characteristics of early hepatocellular carcinoma. *Curr Issues Mol Biol*. 2022;44(10):4714–4734. doi:10.3390/cimb44100322
9. Shi J, Guo W, Jin Y, et al. Recognition of HER2 expression in hepatocellular carcinoma and its significance in postoperative tumor recurrence. *Cancer Med*. 2019;8(3):1269–1278. doi:10.1002/cam4.2006
10. Lokhandwala T, Aly A, Farrelly E, et al. Management of hepatocellular carcinoma from diagnosis in routine clinical practice. *Hepatol Oncol*. 2022;9(4). doi:10.2217/hep-2021-0011

11. Moris D, Martinino A, Schiltz S, et al. Advances in the treatment of hepatocellular carcinoma: an overview of the current and evolving therapeutic landscape for clinicians. *CA Cancer J Clin*. 2025. doi:10.3322/caac.70018
12. Chehelgerdi M, Chehelgerdi M, Allela OQB, et al. Progressing nanotechnology to improve targeted cancer treatment: overcoming hurdles in its clinical implementation. *Mol Cancer*. 2023;22(1):169. doi:10.1186/s12943-023-01865-0
13. Shah KA, Razzaq A, Ali T, et al. Role of nanomedicines in lung cancer treatment and diagnosis: opportunities and challenges. *Med Oncol*. 2025;42(8):305. doi:10.1007/s12032-025-02862-7
14. Malik S, Muhammad K, Waheed Y. Emerging applications of nanotechnology in healthcare and medicine. *Molecules*. 2023;28(18):6624. doi:10.3390/molecules28186624
15. Xu JJ, Zhang WC, Guo YW, Chen XY, Zhang YN. Metal nanoparticles as a promising technology in targeted cancer treatment. *Drug Deliv*. 2022;29(1):664–678. doi:10.1080/10717544.2022.2039804
16. Khursheed R, Dua K, Vishwas S, et al. Biomedical applications of metallic nanoparticles in cancer: current status and future perspectives. *Biomed Pharmacother*. 2022;150:112951. doi:10.1016/j.biopha.2022.112951
17. Samuelian JM, Swanson DA, Kudchadker RJ, et al. Clinical Investigations Long-term tumor control after brachytherapy for base of prostate cancer. *J Contemp Brachyther*. 2011;4:183–187. doi:10.5114/jcb.2011.26468
18. Liu Y, Li J, Chen M, Chen X, Zheng N. Palladium-based nanomaterials for cancer imaging and therapy. *Theranostics*. 2020;10(22):10057–10074. doi:10.7150/thno.45990
19. Nyabadza A, McCarthy É, Makhesana M, et al. A review of physical, chemical and biological synthesis methods of bimetallic nanoparticles and applications in sensing, water treatment, biomedicine, catalysis and hydrogen storage. *Adv Colloid Interface Sci*. 2023;321:103010. doi:10.1016/j.cis.2023.103010
20. Ramalingam V, Raja S, Harshavardhan M. *In situ* one-step synthesis of polymer-functionalized palladium nanoparticles: an efficient anticancer agent against breast cancer. *Dalton Trans*. 2020;49(11):3510–3518. doi:10.1039/C9DT04576G
21. Bellissima A, Cucci LM, Sanfilippo V, et al. Pd-based hybrid nanoparticles as multimodal theranostic nanomedicine. *ACS Appl Bio Mater*. 2023;6(2):483–493. doi:10.1021/acsabm.2c00759
22. Tang D, Chen X, Kang R, Kroemer G. Ferroptosis: molecular mechanisms and health implications. *Cell Res*. 2021;31(2):107–125. doi:10.1038/s41422-020-00441-1
23. Gurunathan S, Kang MH, Jeyaraj M, Kim JH. Palladium nanoparticle-induced oxidative stress, endoplasmic reticulum stress, apoptosis, and immunomodulation enhance the biogenesis and release of exosome in human leukemia monocytic cells (THP-1). *Int J Nanomed*. 2021;16:2849–2877. doi:10.2147/IJN.S305269
24. Jia C, Guo Y, Wu F. Chemodynamic Therapy via Fenton and Fenton-Like Nanomaterials: strategies and Recent Advances. *Small*. 2022;18(6). doi:10.1002/smll.202103868
25. Carpentier A. Cell Culture Models for Hepatitis B and D Viruses Infection: old Challenges, New Developments and Future Strategies. *Viruses*. 2024;16(5):716. doi:10.3390/v16050716
26. Qiu GH, Xie X, Xu F, Shi X, Wang Y, Deng L. Distinctive pharmacological differences between liver cancer cell lines HepG2 and Hep3B. *Cytotechnology*. 2015;67(1):1–12. doi:10.1007/s10616-014-9761-9
27. Mitchell JK, Midkiff BR, Israelow B, et al. Hepatitis C virus indirectly disrupts DNA damage-induced p53 responses by activating protein kinase R. *mBio*. 2017;8(2). doi:10.1128/mBio.00121-17
28. Wei X, Cao W, Wang S, et al. Progress in the application of novel nanomaterials in targeted therapy for liver cancer. *Int J Nanomed*. 2025;20:2623–2643. doi:10.2147/IJN.S509409
29. Gharibkandi NA, Wawrowicz K, Majkowska-Pilip A, Żelechowska-Matysiak K, Wierzbicki M, Bilewicz A. Au@109Pd core–shell nanoparticle conjugated to trastuzumab for the therapy of HER2+ cancers: studies on the applicability of 109Pd/109mAg in vivo generator in combined β− auger electron therapy. *EJNMMI Radiopharm Chem*. 2023;8(1):26. doi:10.1186/s41181-023-00212-4
30. Gharibkandi NA, Majkowska-Pilip A, Walczak R, Wierzbicki M, Bilewicz A. Au@109Pd core–shell nanoparticles conjugated to panitumumab for the combined β−—auger electron therapy of triple-negative breast cancer. *Int J Mol Sci*. 2024;25(24):13555. doi:10.3390/ijms252413555
31. Annamalaisamy GP, Lyczko M, Bilewicz A. The radioactive ^{103}Pd and ^{109}Pd palladium bipyridyl–bisphosphonate complexes for radionuclide therapy of bone metastatic tumor cells. *RSC Adv*. 2025;15(23):18501–18511. doi:10.1039/D5RA02172C
32. Gharibkandi NA, Wawrowicz K, Walczak R, Majkowska-Pilip A, Wierzbicki M, Bilewicz A. 109Pd/109mAg in-vivo generator in the form of nanoparticles for combined β- - Auger electron therapy of hepatocellular carcinoma. *EJNMMI Radiopharm Chem*. 2024;9(1):59. doi:10.1186/s41181-024-00293-9
33. Zilka O, Shah R, Li B, et al. On the mechanism of cytoprotection by ferrostatin-1 and liproxstatin-1 and the role of lipid peroxidation in ferroptotic cell death. *ACS Cent Sci*. 2017;3(3):232–243. doi:10.1021/acscentsci.7b00028
34. Turkevich J, Stevenson PC, Hillier J. A study of the nucleation and growth processes in the synthesis of colloidal gold. *Discuss Faraday Soc*. 1951;11:55. doi:10.1039/df9511100055
35. Wawrowicz K, Majkowska-Pilip A, Gaweł D, Chajduk E, Pieńkowski T, Bilewicz A. Au@Pt core-shell nanoparticle bioconjugates for the therapy of HER2+ breast cancer and hepatocellular carcinoma. model studies on the applicability of 193mPt and 195mPt radionuclides in auger electron therapy. *Molecules*. 2021;26(7):2051. doi:10.3390/molecules26072051
36. Jung SC, Park YK, Jung HY, Kim SC. Effect of stabilizing agents on the synthesis of palladium nanoparticles. *J Nanosci Nanotechnol*. 2017;17(4):2833–2836. doi:10.1166/jnn.2017.13341
37. Szwed M, Torgersen ML, Kumari RV, et al. Biological response and cytotoxicity induced by lipid nanocapsules. *J Nanobiotechnology*. 2020;18(1):5. doi:10.1186/s12951-019-0567-y
38. Øverbye A, Torgersen ML, Sønstevold T, et al. Cabazitaxel-loaded poly(alkyl cyanoacrylate) nanoparticles: toxicity and changes in the proteome of breast, colon and prostate cancer cells. *Nanotoxicology*. 2021:1–20. doi:10.1080/17435390.2021.1924888
39. Kania KD, Wagner W, Pułaski Ł. CdSe/ZnS core-shell-type quantum dot nanoparticles disrupt the cellular homeostasis in cellular blood–brain barrier models. *Int J Mol Sci*. 2021;22(3):1068. doi:10.3390/ijms22031068
40. Wigner P, Zielinski K, Michlewska S, et al. Disturbance of cellular homeostasis as a molecular risk evaluation of human endothelial cells exposed to nanoparticles. *Sci Rep*. 2021;11(1):3849. doi:10.1038/s41598-021-83291-0

41. Kumar R, Gullapalli R. High throughput screening assessment of Reactive Oxygen Species (ROS) Generation using Dihydroethidium (DHE) fluorescence dye. *J Visualized Exp*. 2024;203. doi:10.3791/66238
42. Bębenek W, Gajek A, Marczak A, et al. MK-8776 and olaparib combination acts synergistically in hepatocellular carcinoma cells, demonstrating lack of adverse effects on liver tissues in ovarian cancer PDX model. *Int J Mol Sci*. 2025;26(2):834. doi:10.3390/ijms26020834
43. Rogalska A, Marczak A, Gajek A, et al. Induction of apoptosis in human ovarian cancer cells by new anticancer compounds, epothilone A and B. *Toxicol in vitro*. 2013;27(1):239–249. doi:10.1016/j.tiv.2012.09.006
44. Robaszkiewicz A, Bartosz G, Soszyński M. N-Chloroamino acids mediate the action of hypochlorite on A549 lung cancer cells in culture. *Toxicology*. 2010;270(2–3):112–120. doi:10.1016/j.tox.2010.02.003
45. Szwed M, Michlewska S, Kania K, Szczęch M, Marczak A, Szczepanowicz K. New SDS-based polyelectrolyte multicore nanocarriers for paclitaxel delivery—synthesis, characterization, and activity against breast cancer cells. *Cells*. 2023;12(16):2052. doi:10.3390/cells12162052
46. Dixon SJ, Lemberg KM, Lamprecht MR, et al. Ferroptosis: an iron-dependent form of nonapoptotic cell death. *Cell*. 2012;149(5):1060–1072. doi:10.1016/j.cell.2012.03.042
47. Jeong EM, Shin JW, Lim J, et al. Monitoring glutathione dynamics and heterogeneity in living stem cells. *Int J Stem Cells*. 2019;12(2):367–379. doi:10.15283/ijsc18151
48. Swiss R, Niles A, Cali JJ, Nadanaciva S, Will Y. Validation of a HTS-amenable assay to detect drug-induced mitochondrial toxicity in the absence and presence of cell death. *Toxicol in vitro*. 2013;27(6):1789–1797. doi:10.1016/j.tiv.2013.05.007
49. Sargiacomo C, Stonehouse S, Moftakhar Z, Sotgia F, Lisanti MP. MitoTracker Deep Red (MTDR) Is a metabolic inhibitor for targeting mitochondria and eradicating Cancer Stem Cells (CSCs), with anti-tumor and anti-metastatic activity in vivo. *Front Oncol*. 2021;11. doi:10.3389/fonc.2021.678343
50. Niles AL, Moravec RA, Eric Hesselberth P, Scurria MA, Daily WJ, Riss TL. A homogeneous assay to measure live and dead cells in the same sample by detecting different protease markers. *Anal Biochem*. 2007;366(2):197–206. doi:10.1016/j.ab.2007.04.007
51. Macejova D, Kollar J, Bobal P, Otevrel J, Schuster D, Brtko J. Triphenyltin isoselenocyanate: a novel nuclear retinoid X receptor ligand with antiproliferative and cytotoxic properties in cell lines derived from human breast cancer. *Mol Cell Biochem*. 2024;479(11):3091–3106. doi:10.1007/s11010-023-04914-w
52. Bittremieux M, Mikoshiba K, Bultynck G. Data on cytotoxicity in HeLa and SU-DHL-4 cells exposed to DPB162-AE compound. *Data Brief*. 2017;12:91–96. doi:10.1016/j.dib.2017.03.034
53. An X, Yu W, Liu J, Tang D, Yang L, Chen X. Oxidative cell death in cancer: mechanisms and therapeutic opportunities. *Cell Death Dis*. 2024;15(8):556. doi:10.1038/s41419-024-06939-5
54. Yu Z, Li Q, Wang J, et al. Reactive oxygen species-related nanoparticle toxicity in the biomedical field. *Nanoscale Res Lett*. 2020;15(1):115. doi:10.1186/s11671-020-03344-7
55. Guo Q, Tang Y, Wang S, Xia X. Applications and enhancement strategies of ROS-based non-invasive therapies in cancer treatment. *Redox Biol*. 2025;80:103515. doi:10.1016/j.redox.2025.103515
56. Villalpando-Rodriguez GE, Gibson SB. Reactive Oxygen Species (ROS) regulates different types of cell death by acting as a rheostat. *Oxid Med Cell Longev*. 2021;2021(1). doi:10.1155/2021/9912436
57. Krishnamurthy HK, Pereira M, Rajavelu I, et al. Oxidative stress: fundamentals and advances in quantification techniques. *Front Chem*. 2024;12. doi:10.3389/fchem.2024.1470458
58. Watanabe D, Wada M. Glutathione depression alters cellular mechanisms of skeletal muscle fatigue in early stage of recovery and prolongs force depression in late stage of recovery. *Am J Physiol Regul Integr Comp Physiol*. 2023;325(2):R120–R132. doi:10.1152/ajpregu.00097.2022
59. Wang L, Zhou X, Lu T. Role of mitochondria in physiological activities, diseases, and therapy. *Mol Biomed*. 2025;6(1):42. doi:10.1186/s43556-025-00284-5
60. Xu X, Pang Y, Fan X. Mitochondria in oxidative stress, inflammation and aging: from mechanisms to therapeutic advances. *Signal Transduct Target Ther*. 2025;10(1):190. doi:10.1038/s41392-025-02253-4
61. Kupcho K, Shultz J, Hurst R, et al. A real-time, bioluminescent annexin V assay for the assessment of apoptosis. *Apoptosis*. 2019;24(1–2):184–197. doi:10.1007/s10495-018-1502-7
62. Dixon SJ, Olzmann JA. The cell biology of ferroptosis. *Nat Rev Mol Cell Biol*. 2024;25(6):424–442. doi:10.1038/s41580-024-00703-5
63. Liu F, Wang Q, Ye H, et al. Identification of STAT3 and MYC as critical ferroptosis-related biomarkers in septic cardiomyopathy: a bioinformatics and experimental study. *J Mol Med*. 2025;103(1):87–100. doi:10.1007/s00109-024-02502-z
64. Singal AG, Yarchoan M, Yopp A, Sapisochin G, Pinato DJ, Pillai A. Neoadjuvant and adjuvant systemic therapy in HCC: current status and the future. *Hepatol Commun*. 2024;8(6). doi:10.1097/HC9.0000000000000430
65. Yang C, Zhang H, Zhang L, et al. Evolving therapeutic landscape of advanced hepatocellular carcinoma. *Nat Rev Gastroenterol Hepatol*. 2023;20(4):203–222. doi:10.1038/s41575-022-00704-9
66. Alven S, Gandidzanwa S, Ngalo B, et al. Platinum group metals nanoparticles in breast cancer therapy. *Pharmaceutics*. 2024;16(9):1162. doi:10.3390/pharmaceutics16091162
67. Kang S, Shin W, Kang K, et al. Revisiting of Pd nanoparticles in cancer treatment: all-round excellence of porous Pd nanoplates in gene-thermo combinational therapy. *ACS Appl Mater Interfaces*. 2018;10(16):13819–13828. doi:10.1021/acsami.8b01000
68. Gil YG, Kang S, Chae A, Kim YK, Min DH, Jang H. Synthesis of porous Pd nanoparticles by therapeutic chaga extract for highly efficient tri-modal cancer treatment. *Nanoscale*. 2018;10(42):19810–19817. doi:10.1039/C8NR07172A
69. Sitia L, Sevieri M, Signati L, et al. HER-2-targeted nanoparticles for breast cancer diagnosis and treatment. *Cancers*. 2022;14(10):2424. doi:10.3390/cancers14102424
70. Wu J, Wang M, Pan Y, et al. Synthesis of manganese-oxide and palladium nanoparticles co-decorated polypyrrole/graphene oxide (MnO_2@Pd@PPy/GO) nanocomposites for anti-cancer treatment. *RSC Adv*. 2022;12(37):23786–23795. doi:10.1039/D2RA03860A
71. Ilett M, Naveed E, Roncal-Herrero T, Aslam Z, Micklethwaite S, Hondow N. In situ electron microscopy techniques for nanoparticle dispersion analysis of commercial sunscreen. *J Nanopart Res*. 2023;25(6):122. doi:10.1007/s11051-023-05769-4
72. Rodriguez-Loya J, Lerma M, Gardea-Torresdey JL. Dynamic light scattering and its application to control nanoparticle aggregation in colloidal systems: a review. *Micromachines*. 2023;15(1):24. doi:10.3390/mi15010024

73. Stetefeld J, McKenna SA, Patel TR. Dynamic light scattering: a practical guide and applications in biomedical sciences. *Biophys Rev*. 2016;8(4):409–427. doi:10.1007/s12551-016-0218-6
74. Liu YY, Sun YY, Guo Y, Chen LL, Guo JH, Wang H. Surface charge affects the intracellular fate and clearance dynamics of CdSe/ZnS quantum dots in macrophages. *Nanomaterials*. 2025;15(15):1189. doi:10.3390/nano15151189
75. Porta LC, Campeiro JD, Hayashi MAF. A native CPP from rattlesnake with therapeutic and theranostic properties. In: *Cell Penetrating Peptides: Methods and Protocols*. New York, NY: Springer US; 2022:91–104. doi:10.1007/978-1-0716-1752-6_6
76. Feng X, Xue Y, Gonca S, et al. Ultrasmall superparamagnetic iron oxide nanoparticles for enhanced tumor penetration. *J Mater Chem B*. 2023;11(15):3422–3433. doi:10.1039/D2TB02630A
77. Harush-Frenkel O, Debotton N, Benita S, Altschuler Y. Targeting of nanoparticles to the clathrin-mediated endocytic pathway. *Biochem Biophys Res Commun*. 2007;353(1):26–32. doi:10.1016/j.bbrc.2006.11.135
78. Zhang LW, Monteiro-Riviere NA. Mechanisms of quantum dot nanoparticle cellular uptake. *Toxicol Sci*. 2009;110(1):138–155. doi:10.1093/toxsci/kfp087
79. Awashra M, Młynarz P. The toxicity of nanoparticles and their interaction with cells: an in vitro metabolomic perspective. *Nanoscale Adv*. 2023;5(10):2674–2723. doi:10.1039/D2NA00534D
80. Xuan L, Ju Z, Skonieczna M, Zhou P, Huang R. Nanoparticles-induced potential toxicity on human health: applications, toxicity mechanisms, and evaluation models. *MedComm*. 2023;4(4). doi:10.1002/mco2.327
81. Huang H, Lei P, Yu H, et al. Micro/nano plastics in the urinary system: pathways, mechanisms, and health risks. *Environ Int*. 2024;193:109109. doi:10.1016/j.envint.2024.109109
82. Alkhalidi HM, Zaman U, Khan D, et al. Microwave assisted eco-benign synthesis of novel palladium nanoparticles (ACPs-PdNPs): a new insight into photocatalytic and biomedical applications. *J Mol Liq*. 2023;392:123469. doi:10.1016/j.molliq.2023.123469
83. Shivakumar M, Manjunatha S, Dharmaprakash MS. Biological activity of PdNPs derived from hemicellulose via microwave assisted green synthesis. *Curr Res Green Sustainable Chem*. 2021;4:100150. doi:10.1016/j.crgsc.2021.100150
84. Yuan YG, Peng QL, Gurunathan S. Combination of palladium nanoparticles and tubastatin-A potentiates apoptosis in human breast cancer cells: a novel therapeutic approach for cancer. *Int J Nanomed*. 2017;12:6503–6520. doi:10.2147/IJN.S136142
85. Gurunathan S, Kim E, Han J, Park J, Kim JH. Green chemistry approach for synthesis of effective anticancer palladium nanoparticles. *Molecules*. 2015;20(12):22476–22498. doi:10.3390/molecules201219860
86. Sabaratnam V, Gurunathan S, Raman J, Abd Malek SN, John P. Green synthesis of silver nanoparticles using Ganoderma neo-japonicum Imazeki: a potential cytotoxic agent against breast cancer cells. *Int J Nanomed*. 2013;4399. doi:10.2147/IJN.S51881
87. Zhao R, Xiang J, Wang B, Chen L, Tan S. Recent advances in the development of noble metal NPs for cancer therapy. *Bioinorg Chem Appl*. 2022;2022(1). doi:10.1155/2022/2444516
88. Thapa RK, Soe ZC, Ou W, et al. Palladium nanoparticle-decorated 2-D graphene oxide for effective photodynamic and photothermal therapy of prostate solid tumors. *Colloids Surf B Biointerfaces*. 2018;169:429–437. doi:10.1016/j.colsurfb.2018.05.051
89. Wawrowicz K, Majkowska-Pilip A, Szwed M, Żelechowska-matysiak K, Chajduk E, Bilewicz A. Oxidative status as an attribute for selective antitumor activity of platinum-containing nanoparticles against hepatocellular carcinoma. *Int J Mol Sci*. 2022;23(23):14773. doi:10.3390/ijms232314773
90. Gurunathan S, Qasim M, Park CH, et al. Cytotoxicity and transcriptomic analyses of biogenic palladium nanoparticles in human ovarian cancer cells (SKOV3). *Nanomaterials*. 2019;9(5):787. doi:10.3390/nano9050787
91. Ward A, Hudson JW. p53-dependent and cell specific epigenetic regulation of the polo-like kinases under oxidative stress. *PLoS One*. 2014;9(1):e87918. doi:10.1371/journal.pone.0087918
92. Rodríguez-Hernández MA, Chapresto-Garzón R, Cadenas M, et al. Differential effectiveness of tyrosine kinase inhibitors in 2D/3D culture according to cell differentiation, p53 status and mitochondrial respiration in liver cancer cells. *Cell Death Dis*. 2020;11(5):339. doi:10.1038/s41419-020-2558-1
93. Arzumanian V, Pyatnitskiy M, Poverennaya E. Comparative transcriptomic analysis of three common liver cell lines. *Int J Mol Sci*. 2023;24(10):8791. doi:10.3390/ijms24108791
94. Ondracek CR, Reese VC, Rushing CN, Oropeza CE, McLachlan A. Distinct regulation of hepatitis B virus biosynthesis by peroxisome proliferator-activated receptor γ coactivator 1α and small heterodimer partner in human hepatoma cell lines. *J Virol*. 2009;83(23):12545–12551. doi:10.1128/JVI.01624-09
95. Danjolli-Hashani D, Selen-Isbilir S. Cytotoxic effect of *Cotinus coggygria* extract on Hep3B cancer cell line. *Nat Prod Res*. 2023;37(23):4004–4007. doi:10.1080/14786419.2022.2158462
96. Gripon P, Rumin S, Urban S, et al. Infection of a human hepatoma cell line by hepatitis B virus. *Proc Natl Acad Sci*. 2002;99(24):15655–15660. doi:10.1073/pnas.232137699
97. Gurunathan S, Jeyaraj M, Kang MH, Kim JH. Melatonin enhances palladium-nanoparticle-induced cytotoxicity and apoptosis in human lung epithelial adenocarcinoma cells A549 and H1229. *Antioxidants*. 2020;9(4):357. doi:10.3390/antiox9040357
98. Rokade SS, Joshi KA, Mahajan K, et al. *Gloriosa superba* mediated synthesis of platinum and palladium nanoparticles for induction of apoptosis in breast cancer. *Bioinorg Chem Appl*. 2018;2018:1–9. doi:10.1155/2018/4924186
99. Al-Fahdawi MQ, Rasedee A, Al-Doghachi FA, Rosli R, Taufiq-Yap YH, Al-Qubaisi MS. Anticancer palladium-doped magnesia nanoparticles: synthesis, characterization, and in vitro study. *Nanomedicine*. 2020;15(6):547–561. doi:10.2217/nnm-2019-0178
100. Yaqoob SB, Adnan R, Rameez khan RM, Rashid M. Gold, silver, and palladium nanoparticles: a chemical tool for biomedical applications. *Front Chem*. 2020;8. doi:10.3389/fchem.2020.00376
101. Kesharwani P, Ma R, Sang L, et al. Gold nanoparticles and gold nanorods in the landscape of cancer therapy. *Mol Cancer*. 2023;22(1):98. doi:10.1186/s12943-023-01798-8
102. Luo M, Zhao F, Wang Y, Bian J. Au@Pd nanozyme-mediated catalytic therapy: a novel strategy for targeting tumor microenvironment in cancer treatment. *J Transl Med*. 2024;22(1):814. doi:10.1186/s12967-024-05631-8
103. Wei X, Jiang Y, Chenwu F, et al. Synergistic ferroptosis–immunotherapy nanoplatforms: multidimensional engineering for tumor microenvironment remodeling and therapeutic optimization. *Nanomicro Lett*. 2026;18(1):56. doi:10.1007/s40820-025-01862-6